An unstructured finite volume method based on the projection method combined momentum interpolation with a central scheme for three-dimensional nonhydrostatic turbulent flows

Wei Zhang, Miguel Uh Zapata, Xin Bai, Damien Pham Van Bang, Kim Dan Nguyen

PII: S0997-7546(19)30192-X
DOI: https://doi.org/10.1016/j.euromechflu.2020.06.006
Reference: EJMFLU 103651

To appear in: *European Journal of Mechanics / B Fluids*

Received date : 3 April 2019
Revised date : 21 December 2019
Accepted date : 6 June 2020

Please cite this article as: W. Zhang, M. Uh Zapata, X. Bai et al., An unstructured finite volume method based on the projection method combined momentum interpolation with a central scheme for three-dimensional nonhydrostatic turbulent flows, *European Journal of Mechanics / B Fluids* (2020), doi: https://doi.org/10.1016/j.euromechflu.2020.06.006.

An unstructured finite volume method based on the projection method combined momentum interpolation with a central scheme for three-dimensional nonhydrostatic turbulent flows

Wei Zhang[a], Miguel Uh Zapata[b], Xin Bai[a], Damien Pham Van Bang[c], Kim Dan Nguyen[a,*]

[a]*Laboratory for Hydraulics Saint-Venant, Université Paris-Est, ENPC-EDF-CEREMA, 78400 Chatou, France.*
[b]*CONACYT - Centro de Investigación en Matemáticas A.C, Unidad Mérida, 97302 Mérida, Yucatán, México.*
[c]*Laboratory for Hydraulics and Environment (LHE), Institut National de la Recherche Scientifique, Université du Québec, G1K 9A9, Québec, Canada*

Abstract

This paper presents a three-dimensional nonhydrostatic model to solve the Navier-Stokes equations using an unstructured finite volume method. The physical domain could be geometrically arbitrary. To avoid the checkerboard problem caused by non-staggered grids, a momentum interpolation method is used by introducing face-normal velocities at the mid-points of the cell faces. As the Large Eddy Simulation (LES) requires at least second-order accuracy in time and in space for all the terms, a central scheme combined with an explicit Adams-Bashforth scheme is proposed in this model. The projection method is applied to decouple the velocity field and pressure. Several benchmark test cases are used to validate the second-order accuracy, the numerical stability and the performance of the model. Analysis on divergence noise using an unstructured collocated triangular grid, as well as on the ratio between vertical and horizontal spacing steps have been done to show the reliability of the model. The proposed model has been used to simulate backward-facing step flows, lid-cavity flows, turbulent open channel flows and the turbulent flows around a vertical cylinder. The convergence of the linear solver is analyzed in terms of the iterations and CPU time. The results are fairly in agreement with the references in the literature. The proposed model is able to correctly reproduce the characteristic flow features in all the test cases.

Keywords: Unstructured collocated grid, Finite volume method, Projection method, Momentum Interpolation Method, Large eddy simulation, Nonhydrostatic flow.

---

1. Introduction

Due to the complex physics processes and the limitation of computing power, traditional numerical efforts devoted to the geophysical flow problems, are usually confined into two-dimensional (2D) modeling

---

[*] Corresponding author at: EDF R&D 6, quai Watier, 78400 Chatou cedex, France, Tel.: +33 1 30 87 80 86.
Email address: `kimdan_nguyen@yahoo.fr` (Kim Dan Nguyen)

using the hydrostatic approach [1, 2]. These models can provide rough estimation for future scenarios but lack the capability to handle with three-dimensional (3D) near-field flows such as nonhydrostatic turbulent flows around obstacles in complex geometry. They usually fail in capturing velocity profiles and coherent structure of flows due to the hydrostatic approximation and the absence of correct turbulence modeling [3]. With the development of high performance computer, nowadays LES has been largely used to simulate high turbulent geophysical flows by massive parallel [4, 5, 6].

This paper proposes an accurate, robust and efficient solver for the incompressible Navier-Stokes (N-S) equations using LES in collocated unstructured grids. It is well-known that a collocated grid arrangement for incompressible flows could generate unrealistic pressure oscillations due to the pressure-velocity decoupling, which is known as the checkerboard problem. This problem can be solved using the Momentum Interpolation Method (MIM) [7, 8]. In the past few years, the finite volume method with collocated unstructured grid has been used for both steady and unsteady flows [9, 10, 11, 12]. In these work, the mass flux was calculated by introducing a face-normal velocity, defined at the mid-point of each cell face. This mass flux or the face-normal velocity was interpolated from the cell centers and later corrected by the pressure gradient, which is obtained by the least square method. Depending on the circumstances of different applications, both first order interpolation [13, 14, 15] and second order interpolation [9, 10, 11, 16] could be used.

The originality of this paper is based on the reconstruction of the Projection Methods (PM) using Adams-Bashforth scheme and the Momentum Interpolation Method (MIM) to determine the face-normal velocity combined with central schemes for both convection and diffusion terms. The approximation of the cross diffusion term is improved to handle non-orthogonal, unstructured grids with moderate skewness by introducing an additional correction term. Based on the foregoing method, the second-order accuracy in space and in time is insured in simulating flows at moderate Reynolds numbers.

The structure of the theoretical part is now organized as follows. First, the governing equations including the LES model are presented. The projection method, the time integration, and the finite volume discretization are described in the next section. The numerical results are organized in three sections: accuracy, validation and performance. In the accuracy section, analytical solutions are used to quantify the numerical error of the proposed numerical techniques including the divergence errors, the diffusive and convective terms approximations, and the overall accuracy in time and space. In the validation section, the proposed model is now tested by several well-known benchmarks in comparing the results with experimental solutions, or with other numerical formulations existing in the literature. The test cases include the backward facing step flow, the turbulent channel flow, the lid-driven cavity flow and the flow around a vertical cylinder at a moderate Reynolds number. In the performance section, the convergence of the linear solver is analyzed in terms of iteration numbers and CPU time. Finally, a brief summary and the proposition for future work are also included.

2. Governing equations

The non-dimensional Navier-Stokes equations for unsteady incompressible viscous flow are given by

$$\frac{\partial u_i}{\partial t}+\frac{\partial\left(u_i u_j\right)}{\partial x_j}=-\frac{\partial p}{\partial x_i}+\frac{1}{Re}\frac{\partial^2 u_i}{\partial x_j \partial x_j}+f_i, \tag{1}$$

$$\frac{\partial u_i}{\partial x_i}=0, \tag{2}$$

where the subscripts $i, j = 1, 2, 3$ represent the directions in the Cartesian coordinates, u_i is the non-dimensional velocity component in the x_i direction, p is the non-dimensional pressure, and f_i is an external force. The Reynolds number is defined as $Re = u_{ref} L_{ref}/\nu$ where the reference scales u_{ref} and L_{ref} are for the velocity and length, respectively. The kinematic viscosity is given by $\nu = \mu/\rho$. The fluid is assumed to have a constant density ρ and dynamic viscosity μ. The non-dimensional velocity and pressure are defined as $u_i = (u_i)_{phy}/u_{ref}$, $p = p_{phy}/(\rho u_{ref}^2)$, where $(u_i)_{phy}$ and p_{phy} are the corresponding dimensional velocity and pressure.

2.1. LES turbulence modeling

The Direct Numerical Simulation (DNS) method solves equations (1) and (2) with a suitable numerical technique, introducing no turbulence model. However, such calculations are not feasible for practical flows with high Reynolds numbers. The idea of LES is to apply an implicit spatial filter of characteristic space size to equations (1) and (2). The resulting filtered N-S equations are given by

$$\frac{\partial \bar{u}_i}{\partial t}+\frac{\partial\left(\bar{u}_i \bar{u}_j\right)}{\partial x_j}=-\frac{\partial \bar{p}}{\partial x_i}+\frac{1}{Re}\frac{\partial^2 \bar{u}_i}{\partial x_j \partial x_j}-\frac{\partial \tau_{ij}^{sg}}{\partial x_j}, \tag{3}$$

$$\frac{\partial \bar{u}_i}{\partial x_i}=0, \tag{4}$$

where the bar over any variable denotes filtering, $\bar{u}_i$ are the resolved velocity components of the velocity vector, $\bar{p}$ is the resolved pressure, and

$$\tau_{ij}^{sg}=\overline{u_i u_j}-\bar{u}_i \bar{u}_j, \tag{5}$$

is the Sub-Grid Stress (SGS) tensor used to take into account the effect of unresolved length scales. For simplicity, the external forces are set to be $f_i = 0$.

As suggested by Smagorinsky, the smallest turbulent eddies are almost isotropic and the Boussinesq eddy viscosity assumption can be used to provide an accurate approximation of the effects of these unresolved smallest eddies. According to the Boussinesq assumption, the momentum transfer can be modeled with an eddy viscosity, and equation (5) can be described as

$$\tau_{ij}^{sg}=-2\nu_t \overline{S}_{ij}+\frac{1}{3}\tau_{ii}^{sg}\delta_{ij}, \tag{6}$$

where $\overline{S}_{ij}=\frac{1}{2}\left(\frac{\partial \bar{u}_i}{\partial x_j}+\frac{\partial \bar{u}_j}{\partial x_i}\right)$ is the resolved strain rate-tensor and δ_{ij} is the Kronecker delta.

The SGS viscosity is given by

$$\nu_t = l_{sg}^2 \left|\bar{S}\right|, \quad \left|\bar{S}\right| = \sqrt{2\bar{S}_{ij}\bar{S}_{ij}} \tag{7}$$

where l_{sg} is the sub-grid length scale. In the near wall region, the length scale of the sub-grid scale motions cannot be described with a constant value; it decreases as the wall is approached. Thus, a wall damping function must be additionally implemented to the standard Smagorinsky SGS model in order to capture this boundary layer effect. In the current study, the near wall damping model of Mason and Thomson [17] is used to obtain a modified length scale, described by

$$\frac{1}{l_{sg}^{\mathfrak{n}}} = \frac{1}{(C_s\Delta)^{\mathfrak{n}}} + \frac{1}{(\kappa l_w)^{\mathfrak{n}}}, \tag{8}$$

where $\mathfrak{n} = 2$ is the Mason wall matching power, C_s is the Smagorinsky constant, and Δ is the average spacing $\Delta = V^{1/3}$ with V being the volume of the control cell, κ is the von Kármán constant, and l_w is the distance from the cell center of a control volume to the wall. The value of $C_s = 0.1$ previously proposed for channel flow [18] is used in the current study, where strong anisotropic turbulence occurs in the near-wall region.

The isotropic part in equation (6) containing the sum of the normal stresses τ_{ii}^{sg} is usually added to the filtered pressure term. Thus, the Smagorinsky model can be easily implemented by introducing the total viscosity term $\nu_T = \frac{1}{Re} + \nu_t$ in the momentum equation (3) as follows

$$\frac{\partial u_i}{\partial t} + \frac{\partial (u_i u_j)}{\partial x_j} = -\frac{\partial p}{\partial x_i} + \frac{\partial}{\partial x_j}\left(\nu_T \frac{u_j}{\partial x_j}\right), \tag{9}$$

$$\frac{\partial u_i}{\partial x_i} = 0, \tag{10}$$

For the sake of simplicity, henceforth the bar in the resolved variables are omitted. The technique to discrete equations (9) and (10) is based on a projection method to decouple the velocity and pressure fields. A second-order explicit Adams-Bashforth scheme for the time integration and a finite volume-method on triangular prisms for the space discretization have been used.

2.2. Grid system

A non-staggered unstructured grid system is used in this paper. In a traditional non-staggered grid, all the velocity field and pressure variables are defined at the cell-centered nodes; however, unrealistic pressure oscillations may occur due to pressure-velocity decoupling. In order to avoid this problem, we follow the non-staggered grid formulation proposed by Kim and Choi [9] as shown in Fig. 1 (a). The pressure p and the velocity components u_i are defined at each cell center, and the face-normal velocity is defined as

$$U = (u_i)_{face} n_i, \tag{11}$$

at the mid-point of each cell face. Here, $(u_j)_{face}$ and n_i represent the velocities and the outward-normal unit vector on each face, respectively. It is worth noting that the grid system differs from the standard C-grid staggered discretization, in which only a face-normal horizontal momentum equation is approximated by dotting the face-normal vector [19, 20]. The benefit of the proposed non-staggered grid system is that it is free from the pressure oscillation problem, and simple to implement in comparison with staggered grids, especially for 3D flows [9].

3. Projection method and time integration

The projection method (PM) was initially proposed by Chorin [21] to decouple the velocity and pressure fields. To ensure a second order of accuracy in time, the Adams-Bashforth scheme is applied for the diffusion, convection and pressure terms. Thus, equations (9) and (10) are explicitly approximated in the following form

$$\frac{u_i^{n+1}-u_i^n}{\Delta t} = c_1\, rhs^n + c_2\, rhs^{n-1} - \left(c_1 \frac{\partial p}{\partial x_i}^{n+\frac{1}{2}} + c_2 \frac{\partial p}{\partial x_i}^{n-\frac{1}{2}} \right), \tag{12}$$

where

$$rhs = \frac{\partial}{\partial x_j}\left(\nu_T \frac{\partial u_i}{\partial x_j}\right) - \frac{\partial u_i u_j}{\partial x_j}, \tag{13}$$

superscript n donates the variables at time t^n, $c_1 = 3/2$, $c_2 = -1/2$ and Δt is the time step. In the projection algorithm, which is employed by the method in this paper, the first step calculates an intermediate velocity as follows

$$u_i^* = u_i^n + \Delta t \left(c_1\, rhs^n + c_2\, rhs^{n-1} + c_2 \frac{\partial p}{\partial x_i}^{n-\frac{1}{2}} \right), \tag{14}$$

where u_i^* is an intermediate velocity field. To calculate the new pressure, a Poisson equation for $p^{n+\frac{1}{2}}$ is implicitly obtained by taking the divergence-free condition (10) into

$$u_i^{n+1} = u_i^* - c_1 \Delta t \frac{\partial p}{\partial x_i}^{n+\frac{1}{2}}, \tag{15}$$

which yields

$$\frac{\partial}{\partial x_i}\left(\frac{\partial p}{\partial x_i}^{n+\frac{1}{2}} \right) = \frac{1}{c_1 \Delta t} \frac{\partial u_i^*}{\partial x_i}, \tag{16}$$

where the right-hand side corresponds to the divergence of the intermediate velocity which is calculated using equation (14). Finally, the velocity components at t^{n+1} is calculated from equation (15) and the face-normal velocity is also obtained as

$$U^{n+1} = U^* - c_1 \Delta t \frac{\partial p}{\partial \mathbf{n}}^{n+1}. \tag{17}$$

The intermediate face-normal velocity U^* is obtained by

$$U^* = \widetilde{u}_i^* n_i, \tag{18}$$

where $\widetilde{u}_i$ denotes interpolation from adjacent cell-center velocities. We remark that approximation (17) satisfies the divergence-free condition and it ensures a strong coupling between pressure and velocity.

4. Finite-volume method

A second-order unstructured finite-volume method is chosen to discretize equations (14)-(17). The 3D domain Ω is discretized into triangular elements in the horizontal direction and into layers in the vertical direction. As a consequence the domain is discretized into prisms denoted by V. Thus, each prism-shaped control volume has five faces ($k = 1, 5$): three with vertical orientation (lateral faces) and two with horizontal orientation (top and bottom face). A schematic plot of a control volume and its neighbors are shown in Fig. 1 (b) and (c).

4.1. Discretization

In order to apply a finite-volume method, the integral form of the governing equations is considered. We integrate over a control volume V and apply the divergence theorem (assuming sufficient regularity). The integral form of the convection-diffusion term in equation (14) is given by

$$\int_V rhs\ dV = \oint_S \left(\nu_T \frac{\partial u_i}{\partial x_j} - u_i u_j \right) n_j dS = \oint_S \left(\nu_T \frac{\partial u_i}{\partial \mathbf{n}} - u_i U \right) dS,$$

where S denotes the cell face and $\mathbf{n}$ is the outward-normal unit vector on each face. Last equation was obtained by substituting the face-normal velocity definition (11). Here, $\partial/\partial\mathbf{n}$ represents the outward-normal derivative on the face shared by two elements. The pressure Poisson equation (16) is computed in a similar manner with

$$\oint_S \frac{\partial p}{\partial \mathbf{n}}^{n+\frac{1}{2}} dS = \frac{1}{c_1 \Delta t} \oint_S U^* dS,$$

Note that up to this point we have not introduced any approximation in space. A scheme of second order of accuracy is obtained by applying the mid-point rule integral approximation for the prism control volume and each of its five faces. Thus, a second-order approximation for the cell-center velocities is given by

$$u_i^* = u_i^n + \frac{\Delta t}{m_V} \sum_{k=1}^{5} m_{S_k} \left[c_1 r_f^n + c_2 r_f^{n-1} \right]_k + c_2 \sum_{k=1}^{5} m_{S_k} \left[\frac{\partial p}{\partial \mathbf{n}}_f^{n-\frac{1}{2}} \right]_k , \qquad (19)$$

where $r_f = \nu_T \frac{\partial u_i}{\partial \mathbf{n}}_f - (u_i)_f U_f$ and subscript f indicates that a variable is evaluated at the mid-point on each face S_k ($k = 1, 5$). m_V is the volume of the prism element, and m_S is the area of each face. The Poisson equation reduces to a second-order approximation of the form

$$\sum_{k=1}^{5} m_{S_k} \left[\frac{\partial p}{\partial \mathbf{n}}_f^{n+\frac{1}{2}} \right]_k = \frac{1}{c_1 \Delta t} \sum_{k=1}^{5} m_{S_k} (U_f^*)_k. \qquad (20)$$

After the pressure is calculated and using equation (15), the new velocity at the cell-center is given by

$$u_i^{n+1} = u_i^* - c_1 \frac{\Delta t}{m_V} \sum_{k=1}^{5} m_{S_k} \left(p_f^{n+\frac{1}{2}} n_i \right)_k , \tag{21}$$

where the face-normal pressure p_f is interpolated from the cell-centers. Finally, the face-normal velocity U_f^{n+1} is calculated using equation (17) and the face-normal derivative of the pressure is given as follows

$$U_f^{n+1} = U_f^* - \Delta t \frac{\partial p}{\partial \mathbf{n}}_f^{n+1} . \tag{22}$$

The intermediate face-normal velocity U_f^* is obtained using equation (18) as follows

$$U_f^* = (u_i)_f^* n_i . \tag{23}$$

We remark that the divergence of the intermediate velocity is only employed for the right-hand side of Poisson equation (20). Furthermore, it is approximated using the interpolation of the known velocity values at the cell-centers u_i^* by

$$\int_V \frac{\partial u_i^*}{\partial x_i} dV \approx \sum_{k=1}^{5} m_{S_k} [(u_i)_f^* n_i]_k ,$$

This is an important difference with the staggered grid formulations where the divergence is calulated from previous face-normal velocities [19].

The proposed finite-volume formulation is completed in performing interpolations at the mid-point on each face, using the equations (19)-(23). The values ϕ_f and $\frac{\partial \phi}{\partial \mathbf{n}}_f$ have to be evaluated by using adjacent values, where ϕ is an arbitrary flow variable. In this paper, both ϕ_f and $\frac{\partial \phi}{\partial \mathbf{n}}_f$ are obtained by using the values at neighboring cell centers and vertices, as shown in Fig. 1 (b) and (c).

4.2. Interpolations

In this paper, vertical face interpolations are calculated as a two-dimensional formulation because all the horizontal cell-centers are located at the same height, see Fig. 1. We denote $\mathbf{x}_I$ and $\mathbf{x}_J$ as the cell-centers of the two elements sharing a face. The intersection point between the line connecting these two cell centers and the shared face is denoted by $\mathbf{x}_O$, and the mid-point on each face is denoted by $\mathbf{x}_f$, as shown in Fig. 2. Note that for unstructured grids the point $\mathbf{x}_O$ does not necessarily coincide with the face center $\mathbf{x}_f$ in the horizontal direction.

4.2.1. Values at the cell face

The velocity components $(u_i)_f$ $(i = 1, 2, 3)$ and pressure p at the mid-point of the faces may be approximated in several ways. In this paper, any flow variable ϕ_f is obtained using a second-order interpolation equivalent to a central difference scheme as follows

$$\phi_f = \alpha \phi_I + (1 - \alpha) \phi_J + \frac{1}{2} (\nabla \phi_I + \nabla \phi_J) \cdot \boldsymbol{\varepsilon} , \tag{24}$$

where α is the distance from the normalized distance from the $\mathbf{x}_J$ to the intersection point $\mathbf{x}_O$ ($\alpha = \|\mathbf{x}_J - \mathbf{x}_O\|/\|\mathbf{x}_J - \mathbf{x}_I\|$) and $\boldsymbol{\varepsilon}$ is the vector from the intersection point of the cell-centers and the mid-point of the face ($\boldsymbol{\varepsilon} = \mathbf{x}_O - \mathbf{x}_f$). The gradient at any cell center is calculated using the least squares method presented by Davidson [15]. Note that $\boldsymbol{\varepsilon} = \mathbf{0}$ at the top and bottom faces because $\mathbf{x}_O$ and $\mathbf{x}_f$ are located at the same point.

4.2.2. Normal derivative at the cell face

The outward-normal derivatives on the cell face at the mid-points are approximated as proposed by Kim and Choi [9]

$$\frac{\partial \phi}{\partial \mathbf{n}}_f = \frac{\phi_J - \phi_I}{\delta_{IJ}} + \frac{\phi_{\mathrm{v}_2} - \phi_{\mathrm{v}_1}}{\delta_{\mathrm{v}_1\mathrm{v}_2}} \tan(\theta), \tag{25}$$

where δ_{IJ} is the sum of the normal distances from $\mathbf{x}_I$ and $\mathbf{x}_J$ to the cell face; $\delta_{\mathrm{v}_1\mathrm{v}_2}$ is the distance from the vertex $\mathbf{x}_{\mathrm{v}_1}$ to $\mathbf{x}_{\mathrm{v}_2}$; θ is the angle between the normal vector $\mathbf{n}$ and the line containing $\mathbf{x}_I$ and $\mathbf{x}_J$, as shown in Fig. 2(b). Equation (25) is composed of two terms: the first one corresponds to the principal diffusion and the second one corresponds to the cross diffusion. Note that for orthogonal grids, the cross diffusion is equal to zero as $\theta = 0$. The value of ϕ_{v} at any vertex is obtained by averaging over all surrounding cell centers as follows

$$\phi_{\mathrm{v}} = \frac{\sum\limits_m \omega_m \phi_m}{\sum\limits_m \omega_m}, \tag{26}$$

where $\omega_m = 1/L_m$ is a weighting value, where L_m is the distance between the vertex and the cell center.

The cross diffusion term ensures second-order of accuracy for non-orthogonal unstructured grids with moderate skewness. However, for the problems with high skewness grids, such as a real estuary, this approximation needs to be improved to reach high accuracy. Xue and Barton [22] proposed a new interpolation using the values at a shifted position from the cell center, as shown in Fig. 2(c). Two projected points ($\mathbf{x}_{I'}$ and $\mathbf{x}_{J'}$) parallel to the connecting line are constructed by moving the corresponding cell centers along the distance vector $\boldsymbol{\varepsilon}$. The values of the projected points are obtained by a linear interpolation. Thus, the normal derivative on the face at the mid-point is approximated as follows

$$\frac{\partial \phi}{\partial \mathbf{n}}_f = \frac{(\phi_J + \nabla\phi_J \cdot \boldsymbol{\varepsilon}) - (\phi_I + \nabla\phi_I \cdot \boldsymbol{\varepsilon})}{\delta_{IJ}} + \frac{\phi_{\mathrm{v}_2} - \phi_{\mathrm{v}_1}}{\delta_{\mathrm{v}_1\mathrm{v}_2}} \tan(\theta). \tag{27}$$

In the top and bottom face, $\boldsymbol{\varepsilon} = \mathbf{0}$ and $\theta = 0$ in equations (25) and (27) as $\mathbf{x}_O = \mathbf{x}_f$.

4.3. Pressure linear system and solvers

The intermediate and final velocity field can be explicitly calculated using the proposed PM. The finite-volume discretization for the Poisson equation results in a linear system. Substitution of the interpolation

(25) into (20) yields the discrete Poisson equation for the nonhydrostatic pressure field as follows

$$\sum_{k=1}^{5} \frac{m_{S_k}}{\delta_{IJ_k}} (p_{J_k} - p_I) + \sum_{k=1}^{3} \frac{m_{S_k} \tan(\theta_k)}{(\delta_{\mathrm{v}_1\mathrm{v}_2})_k} (p_{\mathrm{v}_2} - p_{\mathrm{v}_1})_k = \frac{1}{c_1 \Delta t} \sum_{k=1}^{5} m_{S_k} (U_f^*)_k. \tag{28}$$

The resulting linear system is given by

$$A\overrightarrow{p} + \overrightarrow{b_v} = \overrightarrow{r_u}, \tag{29}$$

where the vector $\overrightarrow{p}$ consists of the total unknown variables p_I $(I = 1, \ldots, N_{cell})$ at the cell-centers in the 3D computational domain; the matrix A contains only the coefficients obtained from the geometric values and variables at the cell-centers; the vector $\overrightarrow{b_v}$ contains the values related to the vertices; and the vector $\overrightarrow{r_u}$ corresponds to the known right-hand side related to the intermediate velocity. The vector $\overrightarrow{b_v}$ depends linearly on the solution $\overrightarrow{p}$ as $\overrightarrow{b_v} = B\overrightarrow{p}$, where B is the matrix related to the vertex interpolation and normal-face derivative approximations.

Linear system (29) yields a non-symmetric, sparse matrix in which the bandwidth is a strong function of the ordering of the unstructured cells. In this work, the numerical solutions are performed using the Bi-Conjugate Gradient Stabilized (BICGSTAB) method. The performance analysis of this solver is given in the last section.

4.4. Boundary conditions

Boundary conditions are applied by constructing artificial ghost cells, which are symmetrically opposite to the physical boundaries. For Dirichlet boundaries, the ghost value is calculated by $\phi_{ghost} = 2C - \phi_c$, where C is the exact value given at the boundary. The exact value C is also imposed at the boundary vertices. For Neumann boundaries, the ghost cells are updated using $\phi_{ghost} = \phi_c$, while the values on the boundary vertices are interpolated using only the inner cell-centers. For periodic boundaries, boundary conditions are imposed on two corresponding cells at the inflow and outflow boundary, with $\phi_{out\ ghost} = \phi_{in}$ and at the same time $\phi_{in\ ghost} = \phi_{out}$.

4.5. Numerical Stability

The numerical stability for the present formulation is limited by the explicit discretization of the convection and diffusion terms. In the current study, the Courant-Friedrichs-Lewy (CFL) number is specified according to the original definition given by Kim and Choi [9]

$$CFL = \frac{1}{2}\left(\frac{1}{m_V}\sum_{k=1}^{5} |(U_f)_k m_{S_k}|\right)\Delta t \tag{30}$$

where the sum is taken over the total number of cell faces in a control volume V.

5. Accuracy of the numerical techniques

The accuracy of the proposed numerical method for incompressible turbulent flows depends a great deal on the approximation of the normal velocity and the outward-normal derivative on the face as well as the type of computational grids. In this section, analytical solutions are used to quantify the numerical error of the proposed numerical techniques. First, the divergence approximation is analyzed in order to study the triangular C-grid divergence noise issue. Next, the numerical performance of the face-normal derivative approximation in the diffusion terms is studied for a Poisson problem, and the central scheme for a normal-face value is tested using a pure advection problem. Finally, the overall accuracy of the method in time and space is analyzed using the Taylor decaying vortex problem.

The order of accuracy is defined by

$$\text{order} = \frac{\log\left(\|\cdot\|_{N_1} / \|\cdot\|_{N_2}\right)}{\log\left(N_2/N_1\right)},$$

where $\|\cdot\|_{N_1}$ and $\|\cdot\|_{N_2}$ correspond to norm errors with a resolution associated with grid size N_1 and N_2 respectively. The error is computed using the L_2 and L_∞-norm given by

$$\|e\|_2 = \left[\frac{1}{N_{cell}}\sum_{i=1}^{N_{cell}} e_i^2\right]^{1/2}, \quad \|e\|_\infty = \max_{i=1,N_{cell}} (e_i),$$

respectively. In these equations, N_{cell} is the total number of cell-centers and $e_i = |\phi_{nu} - \phi_{an}|$, where ϕ_{nu} and ϕ_{an} are the numerical and analytical variables, respectively.

In the following examples, structured and unstructured grids are used in the horizontal direction for the numerical simulations. In a structured equilateral grid, all cells are equilateral and have the same size as shown in Fig. 3 (a). For structured right-angled grid, the domain is firstly divided into $N \times N$ uniform rectangles and then each rectangle is split to two isosceles right-angled triangles as shown in Fig. 3 (b). For a fully unstructured grid, triangles point in multiple directions and change size. Unstructured grids have been generated using the free software Blue Kenue developed by the Canadian Hydraulic Centre, National Research Council (1998). Fig. 3 (c) shows an example of these three types of grid.

5.1. Divergence noise analysis

For a triangular grid, the divergence approximation by the face-normal velocities may produce high-frequency checkerboard error patterns. These errors can significantly affect the general solution of the problem [23, 24]. In this example, we first carry out the analysis of the divergence approximation and later the effect in general approximation. To focus on the triangular geometry, the simulations are performed only in 2D along a horizontal plane.

For a generic vector field $\mathbf{u}$, we denote the cell average and discrete divergence operator over a cell A as follows

$$\overline{\nabla \cdot \mathbf{u}} = \frac{1}{m_A} \int_A \frac{\partial u_i}{\partial x_i} ds = \frac{1}{m_A} \sum_{j=1}^{3} \left[\int_L (u_i n_i) dl \right]_j , \tag{31}$$

and

$$\operatorname{div}(\mathbf{u}) = \frac{1}{m_A} \sum_{j=1}^{3} [\Delta l \, (u_i)_f n_i]_j = \frac{1}{m_A} \sum_{j=1}^{3} [\Delta l \, U_f]_j , \tag{32}$$

respectively, where m_A stands for the area of the cell and Δl is the length of the triangle edge L. As presented by Wan et al. [23], a truncation error analysis can be performed to show the checkerboard error patterns of the divergence operator on equilateral triangular grids ($\Delta l = \Delta x$). It can be proved that $\operatorname{div}(\mathbf{u})$ is a first-order approximation of both $\overline{\nabla \cdot \mathbf{u}}$ and $(\nabla \cdot \mathbf{u})_c$, where the subscript $()_c$ denotes the value evaluated at the triangle center. More importantly, the first-order error term changes sign from an upward-pointing triangle to a downward-pointing one, which results in a checkerboard error pattern.

The order and checkerboard behavior are studied by performing different numerical simulations with the vector field

$$\mathbf{u} = \frac{1}{2\sqrt{2\pi}} \left(\frac{\sqrt{105}}{2} \cos(2x) \cos^2(y) \sin(y), \, -\sqrt{15} \cos(x) \cos(y) \sin(y) \right) ,$$

and the analytic divergence solution

$$\nabla \cdot \mathbf{u} = -\frac{1}{2\sqrt{2\pi}} \left(\sqrt{105} \sin(2x) \cos^2(y) \sin(y) + \sqrt{15} \cos(x) \cos(2y) \right) .$$

over the computational domain $[0, 2\pi] \times [-\frac{\pi}{2}, \frac{\pi}{2}]$. The discrete divergence, $\operatorname{div}(\mathbf{u})$, is calculated by evaluating the velocity field at the cell centers and then approximating U_f by the central interpolation (24). The numerical solution is compared against the divergence at cell-centers, $(\nabla \cdot \mathbf{u})_c$. For this case, the numerical error analysis confirms that the divergence operator (32) yields a first-order checkerboard error pattern, as shown in Fig. 4 (a), (c) and Table 1. The results are nearly identical to the ones presented by Wan et al. [23]. It is expected as the central interpolation in equilateral grids is reduced to an average value between the two surrounding neighbors.

Table 1: Convergence analysis of the divergence term at the cell-centers and vertices.

Grid		$\operatorname{div}(\mathbf{u})$				$\mathcal{F}[\operatorname{div}(\mathbf{u})]$			
N	Δl	L_∞-norm	Order	L_2-norm	Order	L_∞-norm	Order	L_2-norm	Order
16	0.418	2.71×10^{-1}	—	1.08×10^{-1}	—	2.90×10^{-1}	—	1.22×10^{-1}	—
32	0.202	1.27×10^{-1}	1.09	5.03×10^{-2}	1.10	7.75×10^{-2}	1.90	3.24×10^{-2}	1.91
64	0.099	6.11×10^{-2}	1.06	2.49×10^{-2}	1.01	1.93×10^{-2}	2.01	8.19×10^{-3}	1.98
128	0.049	2.99×10^{-2}	1.03	1.22×10^{-2}	1.03	4.77×10^{-3}	2.02	2.04×10^{-3}	2.01
256	0.024	1.48×10^{-2}	1.01	6.09×10^{-3}	1.00	1.19×10^{-3}	2.00	5.10×10^{-4}	2.00

The checkerboard error pattern can be avoided by applying explicit or implicit filtering operations [24]. In this paper, we improve the divergence operator by using the values located at the vertices. This is equivalent to a Shapiro first-order implicit nodal filter using node downsampling and upsampling [24]. Smoothed values are interpolated back onto cell centers via the Barycentric interpolation, one third of the sum of the vertex values (filtering technique), as follows

$$\mathcal{F}[\mathrm{div}(\mathbf{u})](\mathrm{x}_c) = \frac{1}{3}\sum_{j=1}^{3} \mathrm{div}(\mathbf{u})(\mathbf{x}_{\mathrm{v}j}). \tag{33}$$

where the vertex value $\mathrm{div}(\mathbf{u})(\mathbf{x}_{\mathrm{v}j})$ is calculated by a distance-weighted averaging of the cell-center values using equation (26). Thus, the stencil will be enlarged to all cells sharing a vertex (13 cell-centers for equilateral grids). Note that as cell-center velocities are available in the proposed formulation, we do not need to downsample face-normal velocities onto cell centers with any cell-center velocity reconstruction such as the filtering techniques proposed by Perot [25]. The numerical solution and errors using the filtering technique are shown in Fig. 4 (b) and (d). Note that all checkerboard errors are already eliminated. Furthermore, the method is now second-order accurate as shown in Table 1. Numerical results also show that the discrete divergence at the vertices given by $\mathrm{div}(\mathbf{u})(\mathbf{x}_\mathrm{v})$ is already a second-order approximation of $(\nabla \cdot \mathrm{u})_\mathrm{v}$.

The divergence errors due to the use of unstructured grids present similar checkerboard behavior as compared with the structured grid, see Fig. 5 (a). In particular, the checkerboard patterns are more distinct in regions with distortion. However, the employment of filter technique (33) eliminates the divergence noise even for unstructured grids, as shown in Fig. 5 (b). Numerical results are also more accurate using this filter. Note that the largest errors are concentrated close to the boundary; it is expected as less number of cell-centers are available for the vertex calculation.

In a classic finite volume C-grid staggered approach, vertical velocities are constructed using cell-center horizontal divergences [19, 20]. Consequently, divergence errors are projected onto the vertical velocity. However, in the MIM, the vertical velocity is calculated using the gradient of the known pressure as described in equations (21) and (22). The checkerboard error pattern enters the proposed nonhydrostatic model system by the discrete Poisson equation for the nonhydrostatic pressure (20) and by the velocity convective fluxes in equation (19). However, the divergence term is used explicitly only in computing of the right-hand side of the Poisson equation.

In order to show the possible effect of the divergence errors in the pressure and velocity field approximation, we consider the two-dimensional decaying Taylor vortex test case. The equations are solved on the square domain $[-1, 1] \times [-1, 1]$ which exact velocity field and pressure are given by

$$\begin{aligned} \mathbf{u} &= (-\cos(\pi x)\sin(\pi y),\ \sin(\pi x)\cos(\pi y))\, e^{-\frac{2\pi^2 t}{Re}}, \\ p &= -\tfrac{1}{4}\left(\cos(2\pi x) + \cos(2\pi y)\right) e^{-\frac{4\pi^2 t}{Re}}. \end{aligned} \tag{34}$$

In this test, starting from $t = 0$ and a constant time step is used $\Delta t = 0.001$. An intermediate velocity field is obtained by solving equation (19). In this case, the right-hand side of the convection-diffusion equation is updated using the variables at time t^n. Then, the divergence of this velocity is calculated with the filtering technique or not. Next, the pressure is calculated using the Poisson equation (20). Finally, the new velocity is update by equation (21).

Numerical solution of the divergence of the intermediate velocity field, of the pressure and velocity magnitude for the 2D Taylor Vortex problem are shown in Fig 6. If the filter is not applied, then a checkerboard error pattern is observed in the divergence approximation which is also projected to the numerical solution of the pressure. On the other hand, the filtered solution eliminates the checkerboard pattern and decreases the magnitude of the horizontal divergence field. Note that the largest errors are located close to the boundary as previously discussed. However, the numerical solution of the velocity field for both calculations looks alike. In fact the maximum difference between them is 2.85×10^{-3}. The reduction in the noise can be related to the method used to calculate the pressure gradient in the final step. More details about the accuracy of the Taylor vortex problem will be investigated in Section 5.4.

Although, the proposed filtering strategy can be computed in the pressure step, it cannot directly be employed in the nonlinear convection terms (velocity field computations are combined with the scalar interpolation). In this case, an alternative is to filter the velocity components in hopes that the resultant approximation adequately smooths the divergence field [24]. It is important to note that the face-normal velocity U^n applied in the convective fluxes satisfies the divergence free condition, $\int_L U^n dl = 0$ because it is obtained from equation (22) rather than interpolation from adjacent cell-center velocities u_i. This property may help to the noise reduction of the discrete divergence calculation. Further discussions in this direction will be included in a future paper.

5.2. Poisson problem

Now, the numerical methods for the normal face derivative approximations (25) are tested using the pressure Poisson equation

$$\frac{\partial}{\partial x_i}\left(\frac{\partial \phi}{\partial x_i}\right) = f, \tag{35}$$

where f is a given right-hand side term and Ω is the rectangular domain $[-1,1] \times [-1,1] \times [-1,1]$. The right-hand side function and its corresponding analytical solution are given by

$$f = -\frac{3}{4}\pi^2 \sin\left(\frac{\pi}{2}x\right)\sin\left(\frac{\pi}{2}y\right)\sin\left(\frac{\pi}{2}z\right), \tag{36}$$

and

$$\phi = \sin\left(\frac{\pi}{2}x\right)\sin\left(\frac{\pi}{2}y\right)\sin\left(\frac{\pi}{2}z\right), \tag{37}$$

respectively. Dirichlet boundary conditions are imposed at all boundaries. This example examines the method's capacity for simulating problems with different grid type and resolution. The simulations have been performed using the BICGSTAB solver with a tolerance value of 10^{-5}. At the end of this paper, we study the efficiency of our numerical simulations with iterations and CPU time.

Three types of grid are used in example (36)-(37), as illustrated in Fig. 3. Table 2 shows the number of vertices and cell-centers used to discretize the domain $[-1,1]\times[-1,1]$. Here, Δx is the length of the triangle in the x-direction. In the case of the unstructured grid, it was generated by taking a mean triangle edge close to Δx. The triangles in the horizontal plane are extended in the form of prism for the 3D domain in N_z layers.

Table 2: Size of the structured and unstructured grids used in numerical experiments for the horizontal computational domain.

Grid		Structured equilateral		Structured right-angled		Unstructured	
N	Δx	Vertices	Cells	Vertices	Cells	Vertices	Cells
16	1.33×10^{-1}	295	522	256	450	256	450
32	6.45×10^{-2}	1166	2196	1024	1922	1188	2234
64	3.18×10^{-2}	4636	9000	4096	7938	4752	9234
128	1.56×10^{-2}	18743	36938	16384	32258	18355	36121
256	7.81×10^{-3}	75373	149646	65536	130050	72351	143473

The three-dimensional numerical solution and absolute errors at $z=0.5$ for equilateral and unstructured grids are shown in Fig. 7 using $N=32$. The results demonstrates that the proposed method approximates accurately the exact solution, as expected. Although, the largest errors are located close to the highest values of the forcing function for both types of grids, the absolute error behaves different in both cases. The errors are smoothly distributed for structured grids. However for an unstructured grid, triangles change size and clusters of five, six, or seven cells share a vertex, making the errors larger in some regions than others. The full convergence analysis of the numerical solution of the Poisson equation using structured grids is shown in Table 3. The errors are measured in the Euclidean and maximum norm at all grid points for $N=N_x=N_z$. In all the cases, the results show a good approximation of the numerical solution and the convergence analysis indicates that the method is of second order of accuracy. Note that the errors and order of accuracy of both structural grids are almost the same.

Table 3: Convergence analysis for the 3D pressure Poisson test case using structured grids.

	Structured equilateral grid				Structured right-angled grid			
N	L_∞-norm	Order	L_2-norm	Order	L_∞-norm	Order	L_2-norm	Order
16	3.82×10^{-3}	—	1.08×10^{-3}	—	3.63×10^{-3}	—	1.12×10^{-3}	—
32	1.04×10^{-3}	1.87	2.55×10^{-4}	2.08	1.00×10^{-3}	1.86	2.61×10^{-4}	2.10
64	2.74×10^{-4}	1.92	6.17×10^{-5}	2.04	2.69×10^{-4}	1.89	6.30×10^{-5}	2.05
128	7.09×10^{-5}	1.95	1.53×10^{-5}	2.01	7.01×10^{-5}	1.94	1.55×10^{-5}	2.02

The convergence analysis for unstructured grids is shown in Table 4. This table also shows the influence of the cross diffusion term in discretizing the Poisson equation. The analysis of this term is not necessary for structured grids as the intersection point of the cell-centers and the mid-point of the face are the same ($\mathbf{x}_O=\mathbf{x}_f$). A loss of accuracy is immediately observed without the cross diffusion. Furthermore, norm errors can be larger using a finer grid, as the numerical result for $N=64$ demonstrates. More accurate results are obtained using the approximation including the cross diffusion, as expected. The order of accuracy is second-order using the L_2-norm as it measures a global average error. However, the order of accuracy using the maximum norm decreases as finer grids are used. It is because the unstructured grid is not homogeneous; thus the error is directly related to the particular distribution and the size of the elements in the unstructured grid.

Table 4: Convergence analysis for the 3D pressure Poisson equation using unstructured grids.

	Without cross diffusion		With cross diffusion			
N	L_∞-norm	L_2-norm	L_∞-norm	Order	L_2-norm	Order
16	2.63×10^{-2}	5.38×10^{-3}	4.90×10^{-3}	—	1.21×10^{-3}	—
32	7.55×10^{-3}	8.41×10^{-4}	1.12×10^{-3}	2.13	2.63×10^{-4}	2.20
64	4.88×10^{-3}	1.40×10^{-3}	3.00×10^{-4}	1.90	6.44×10^{-5}	2.03
128	9.76×10^{-3}	2.38×10^{-3}	1.01×10^{-4}	1.57	1.68×10^{-5}	1.94

The approximations in the vertical direction are not calculated in the same way as the horizontal one. Thus, the magnitude of the errors should be different in both directions. Fig. 8 shows the norm errors for structured and unstructured horizontal grids as the vertical resolution (N_z) is increased. The hydrostatic solver perform well for a wide range of the grid aspect ratio $R = \Delta x/\Delta z$ values. Note that for the structured equilateral grid, N_z should be the double of N_x to obtain the minimum error for the 3D Poisson problem. This can be explained as the approximation of the outward-normal derivative is based on the distance from the cell-center to the face cell: $0.5\Delta z$ at the top and bottom faces, and $\frac{1}{3}\frac{\sqrt{3}\Delta x}{2} \approx 0.28\Delta x$ at the faces in the horizontal direction. However, $N_z = N_x$ already gives a precise solution as previously shown in Table 3. In the case of unstructured grids, the horizontal approximations dominates the global accuracy for values $\Delta x/\Delta z \approx 1$, as shown in Fig. 8.

It is important to remark that the numerical solution is still accurate for the grid aspect ratio $R \gg 1$. For example, Fig. 9 shows the numerical solution with a different uniform vertical resolution containing $N_z = 32$, 128 and 512 points, such that R varies from 2 to 34. In order to better understand these results, let us consider a grid of equilateral triangles and a homogeneous discretization in the $z-$direction. In this case, the Poisson equation (28) is reduced to

$$\frac{\Delta z}{\sqrt{3}/3}\sum_{k=1}^{3}(p_{J_k} - p_I) + A\left(\frac{p_{J_T} - p_I}{\Delta z}\right) + A\left(\frac{p_{J_B} - p_I}{\Delta z}\right) = f_I, \tag{38}$$

where I and J refers to the cell center and neighbor cells, respectively, and f_I is the corresponding discretization of the right-hand side of the Poisson equation. Substituting the value of the cell area, the system is equivalent to

$$p_I + a_H\left(p_{J_1} + p_{J_2} + p_{J_3}\right) + a_V\left(p_{J_T} + p_{J_B}\right) = \frac{1}{a_0}f, \tag{39}$$

where

$$a_H = -\left(\frac{1}{3 + \frac{1}{2}R^2}\right), \qquad a_V = -\frac{1}{2}\left(\frac{\frac{1}{2}R^2}{3 + \frac{1}{2}R^2}\right), \qquad a_0 = -\sqrt{3}\Delta z\left(3 + \frac{1}{2}R^2\right), \tag{40}$$

Note that the resulting matrix is diagonally dominant and the horizontal coefficients are smaller than those of the vertical by an amount of $\frac{1}{4}R^2$. Moreover, if $R \to \infty$ (corresponding to the hydrostatic limit), then $a_H \to 0$ and $a_V \to -\frac{1}{2}$. It means that equation (39) degenerates to a tridiagonal linear system; however, the condition number of the corresponding matrix becomes larger. Table 5 shows the condition number[1] of the 3D global matrix varying the number of layers in the vertical direction. The missing values for $N_x = 16$ are due to a computational restriction to storage the full matrix. Note that both a_H and a_V agree with the coefficients in equation (40). More important, the solver still converges to the exact solution for structured and unstructured grids even the condition number on the Poisson problem degrades, as shown in Fig. 8 and Fig. 9.

Table 5: Condition number analysis for the 3D pressure Poisson equation using equilateral grids and varying the number of layers in the vertical direction.

	$\Delta x = 0.285$ ($N_x = 8$)				$\Delta x = 0.133$ ($N_x = 16$)			
N_z	$\Delta x/\Delta z$	a_H	a_V	Con$_{3D}$	$\Delta x/\Delta z$	a_H	a_V	Con$_{3D}$
8	1.00	-2.85×10^{-1}	-0.071	86.34	0.46	-3.21×10^{-1}	-0.017	354.10
16	2.14	-1.88×10^{-1}	-0.216	126.13	1.00	-2.85×10^{-1}	-0.071	385.00
32	4.42	-7.80×10^{-2}	-0.382	299.13	2.06	-1.94×10^{-1}	-0.207	554.70
64	9.00	-2.29×10^{-2}	-0.465	1007.06	4.20	-8.46×10^{-2}	-0.373	1265.62
128	18.14	-5.96×10^{-3}	-0.491	3860.59	8.46	-2.57×10^{-2}	-0.461	—
256	36.42	-1.50×10^{-3}	-0.497	15362.49	17.00	-6.77×10^{-3}	-0.489	—

5.3. Advection problem

This test aims to check the performance of the proposed central scheme (24) as well as the type of grid used for a pure advection problem. The governing equation is given by

$$\frac{\partial \phi}{\partial t} + \frac{\partial (u_j \phi)}{\partial x_j} = 0, \tag{41}$$

where ϕ is the unknown variable, and u_j is a prescribed flow field. For all of the test simulations, the computational domain is set as $[-1, 1] \times [-1, 1] \times [-1, 1]$. Dirichlet boundary conditions are imposed at all boundaries. The numerical performance is quantified for the solid-body cosine bell example. The initial condition and velocity field are given by

$$\phi_1(\mathbf{x}) = \begin{cases} \cos^2(2\pi r), & r \leq \frac{1}{4}, \\ 0, & r > \frac{1}{4}, \end{cases} \tag{42}$$

and

$$\mathbf{u} = \frac{2\pi}{\sqrt{3}} \left(z - y, x - z, y - x\right), \tag{43}$$

respectively, where $r = \|\mathbf{x} - \mathbf{x}_c\|$ and $\mathbf{x}_c = \left(-\frac{1}{2\sqrt{2}}, \frac{1}{2\sqrt{2}}, -\frac{1}{2\sqrt{2}}\right)$. A full revolution is completed at $t = 1.0$. The computational domain is divided into different grid resolutions ($N_x = N_y$) in the horizontal direction

---

[1] The condition number was estimated using the *condest* function of the MATLAB sofware

and N_z vertical layers. The total number of elements ($N = N_x = N_y = N_z$) are ranging from 65,536 ($N = 32$) to 33,554,432 ($N = 256$) using structured right-angled grids. A constant time step, $\Delta t = 10^{-4}$, is used in all simulations in this section.

The numerical solution at different time stages are shown in Fig. 10. The grid resolution corresponds to $N = 128$ using right-angled triangles. Note that the scheme recovers the shape of the sphere when it moves around the domain. Details about the absolute errors after one revolution in coarse mesh at $z = -1/(2\sqrt{2})$ are also given in Fig. 10. Note that structured and unstructured grids have the same error behavior. Table 6 shows the accuracy using L_∞- and L_2-norm error for the right-angled grids. The central scheme exhibits a very good performance in terms of absolute error. Results shows that the numerical errors become closer to a second order of accuracy by increasing the grid resolution. The peak values are also shown in Table 6; they are calculated based on the vertex values resulting from the interpolation of surrounding cell-center values. The peak values are accurately recovered in all cases. Note that the proposed numerical method still exhibits a high peak value even with a low grid resolution. By increasing the grid resolution, the peak value is closer to the exact one.

Table 6: Convergence analysis for the 3D cosine bell test case using structured grids.

	Right-angled grid						
	L_∞-norm		L_2-norm		Peak value		
N	Error	Order	Error	Order	Numerical	Exact	Absolute error
32	7.21×10^{-1}	—	2.69×10^{-2}	—	0.45942	0.99980	5.40×10^{-1}
64	4.15×10^{-1}	0.80	1.34×10^{-2}	1.01	0.88425	0.98435	1.00×10^{-1}
128	1.46×10^{-1}	1.51	4.32×10^{-3}	1.63	0.99561	0.99993	4.32×10^{-3}
256	3.96×10^{-2}	1.88	1.35×10^{-3}	1.68	0.99684	0.99870	1.86×10^{-3}

For non-quasi uniform unstructured grids, the numerical approximation using the central scheme is more sensitive to the grid deformations in terms of size and shape. This problem can be better understood if we focus only on the two-dimensional horizontal plane where the unstructured formulation is applied. As a demonstration, we simulate the 2D cosine bell example, the center location of which is $x_c = (-\frac{1}{2}, 0)$ and the velocity field is given by $\mathbf{u} = (-2\pi y, 2\pi x)$. The mesh and the numerical solution for $N = 32$, 64 and 128 are illustrated in Fig. 11. As expected, the proposed techniques can simulate the cosine bell on general unstructured grids. Table 7 shows the errors after one revolution using the L_∞- and L_2-norm, and the peak values for different grid resolutions. Note that the errors are small and peak values are recovered. Although peak values decreases, they keep close to one as the simulations go forward in time, see Fig. 12.

Table 7: Convergence analysis for the 2D cosine bell test case using unstructured grids.

	Unstructured grid		Peak values		
N	L_∞-norm	L_2-norm	Numerical	Exact	Absolute error
32	5.47×10^{-1}	7.47×10^{-2}	0.70260	0.96758	2.64×10^{-1}
64	2.95×10^{-1}	3.57×10^{-2}	0.91102	0.99295	8.15×10^{-2}
128	7.17×10^{-1}	7.16×10^{-3}	0.95130	0.99829	4.69×10^{-2}

For unstructured grids, we remark that the largest errors of numerical solutions are located in regions where cell sizes rapidly change. If this change in size is too large or the number of cells sharing a vertex varies a lot, then the solution may become unstable. In this paper, besides structured grids, unstructured grids are selected so that smooth transitions between cells are preserved.

Finally, although the central scheme accurately solves the cosine bell example, the scheme is restricted to regular solutions. Discontinuous problems may present spurious oscillations near sharp gradients. Instead of the central scheme, discontinuous problems can be solved by the introduction of a second-order upwind scheme with a flux-limiter technique as described in [26, 27].

5.4. Taylor vortex problem

Finally, the decaying Taylor vortex test case aims to investigate the overall temporal and spatial accuracy of the proposed method in solving the N-S equations. The temporal and spacial convergence analysis is initially studied using the analytical solution given by equation (44) on the same computational domain. In this way, we can only focus in the performance of the horizontal approximation using triangular grids. The Reynolds number for the 2D simulation is set as $Re = 20$. To check the spatial accuracy, different grids are used ranging from $\Delta x = 0.1$ ($N = 20$) to 0.0083 ($N = 240$) while a fixed time step $\Delta t = 0.015$ is used for all simulations. To check the temporal accuracy, five different time steps are used, ranging from $\Delta t = 0.015$ to 0.1, but keeping the mesh size constant. Here, the grid corresponding to $N = 240$ is used to minimize the spatial error. Only five vertical layers are used in the vertical direction. The numerical velocity field is compared with the analytical solution at $t = 0.5$. The numerical results show that the proposed numerical scheme has clearly the second-order accuracy for both spatial and temporal discretization, as shown in Fig. 13.

The N-S equations are also studied on the cubic domain $[0, 2\pi] \times [0, 2\pi] \times [0, 2\pi]$ using the analytical solution

$$\begin{aligned} u &= -\tfrac{1}{2}(\sqrt{3}\cos(\pi x)\sin(\pi y)\sin(\pi z) + \sin(\pi x)\cos(\pi y)\cos(\pi z))e^{-\frac{3\pi^2 t}{Re}}, \\ v &= -\tfrac{1}{2}(\sqrt{3}\sin(\pi x)\cos(\pi y)\sin(\pi z) - \cos(\pi x)\sin(\pi y)\cos(\pi z))e^{-\frac{3\pi^2 t}{Re}}, \\ w &= \cos(\pi x)\cos(\pi y)\sin(\pi z)e^{-\frac{3\pi^2 t}{Re}}, \\ p &= -\tfrac{1}{2}\left(u^2 + v^2 + w^2\right). \end{aligned} \tag{44}$$

This solution, firstly derived in [28], is a 3D generalization of the 2D Taylor vortex problem presented before. Initial conditions are based on the exact solution and periodic boundary conditions are imposed at all the boundaries. We solve the 3D Navier-Stokes equations with $Re = 1600$. The evolution of the iso-surface of the z-component of vortices for a grid resolution of $N = 128$ and $\Delta t = 0.001$ is shown in Fig. 14. The rectangular domains use a structured right-angled grid of resolution N and N sub-divisions of the $z-$direction. As expected, the numerical solution approximates quite well the velocity field. Similarly to the decaying homogeneous turbulence, the flow transits to turbulence with the creation of small scales followed by a decay phase.

6. Validation test cases

In this section, the proposed model is tested with several benchmark problems using experimental solutions or numerical simulations from other authors to quantify the numerical error.

6.1. Backward-facing step flow

For the first test case, we select the flow behind a backward-facing step in a channel. It is a widely used benchmark problem to examine the accuracy of numerical methods for DNS. In this case, the 2D computational domain is set as $[0, 30h] \times [0, 2h]$, where $h = 0.5$ is the step height, so the expansion ratio is 1 : 2. A grid resolution of 600 × 50 triangles is used in this example. A fully developed parabolic velocity profile $u = 24y(0.5 - y)$ and $v = 0$ is prescribed at the inlet ($x = 0$) above the step. No-slip boundary conditions are imposed along the step and the channel walls, and Neumann boundary conditions are used at the outflow boundary. Calculations are performed at $Re = 100$, 200, 400, 600, and 800, where $Re = U_{avg}(2h)/$ and U_{avg} is the bulk velocity. The time step is fixed at $\Delta t = 0.01$.

Fig. 15 shows the calculated reattachment length as a function of the Reynolds number. The numerical results are compared with previous results presented by Armaly et al. [29], Kim and Moin [30], Lee and Mateescu [31] and Williams and Baker [32]. Note that the solution of the proposed numerical formulation are in good agreement with the computational results of Williams and Baker [32] for all the Reynolds numbers calculated. However, at $Re > 400$, a difference exists between the computational and experimental results. This difference results from the three-dimensionality of the flow as Armaly et al. [29] pointed out. At $Re > 400$, a secondary separation bubble exists on the upper wall (see Fig. 16).

6.2. Turbulent channel flow

In order to further validate the proposed model, particularly its behavior in simulating turbulent flows, test cases of open channel flow is done using DNS and LES. This test case represents a great interest to the engineering and scientist community, as most applications can be simplified into either circular or rectangular in cross section. This can also serve as the first step to model real rivers and estuarine flows. Periodic boundary condition is applied in the streamwise and spanwise directions and a constant body force $f_x = 1.0$ is used to drive the flow. No-slip boundary condition is used on bottom and free-slip boundary on top. The initial velocity fields are set as random perturbation field.

6.2.1. DNS of turbulent channel flow

The Reynolds number based on the friction velocity ($Re_\tau = u_\tau h/\nu$) is set as 180 to match the Kim et al. [30], where h is half channel depth. The computational domain is set as $[0, 6h] \times [0, 4h] \times [0, 2h]$ in x, y, z direction, respectively. The horizontal plane is discretized on structured triangle grid of 128×84 with 128 irregular vertical layers. The values of the grid spacing in terms of wall units is $\Delta x^+ = 16, \Delta y^+ = 11$ and $\Delta z^+_{max} = 4.2$. The center of the first layer grids is located at $z^+ \approx 0.7$, which is within the laminar boundary layer. The time step is fixed at $\Delta t = 3 \times 10^{-4}$ to keep the Courant number smaller than 1.0 during the whole simulation. The plane-averaged turbulence statistics values are gathered from $t^+ = 70$ to $t^+ = 100$.

The mean velocity profile at different vertical layers is shown in Fig. 17 (a) along with the reference DNS data of Kim et al. [30]. In general, the current result exhibits good capability in capturing the mean flow field, with the first point sits in the viscous sub-layer. In the buffer region, small discrepancy with the reference data can be observed in this region with a smaller mean velocity. In the region ($z^+ > 20$), the computed results closely follow the log-law, denoting a fully developed turbulent flow. Clearly, DNS results show the capability of the model in simulating turbulence. Using the iso-surface Q-criterion of instantaneous flow, Fig. 17 (b) shows the tube-like vertical structures, which are randomly distributed over the turbulent flow field.

6.2.2. LES of turbulent channel flow

Large eddy simulation is done at the friction Reynolds number as 395. Computations have been performed using the constant coefficient Smagorinsky sub-grid scale model ($C_s = 0.1$). The computational domain is $[0, 2\pi h] \times [0, \pi h] \times [0, 2h]$ in x, y, z direction and discretized by two computational grids $N = 64$ and $N = 96$, respectively. Vertically, a normal irregular grid is given by a hyperbolic-tangent type stretching function:

$$z(j) = \frac{\tanh\left((2.25\left(\frac{2j}{N} - 1\right)\right)}{\tanh(2.25)}, \quad j = 0, 1, \dots, N \tag{45}$$

The grid spaces for coarse mesh are $\Delta x^+ = 38$, $\Delta y^+ = 19$ and the first mesh point away from the wall is at $z^+ \approx 1.4$ and $\Delta z^+_{max} = 28.2$; while for fine mesh, the grid spaces are $\Delta x^+ = 16$, $\Delta y^+ = 13$, $\Delta z^+_{min} = 0.86$, $\Delta z^+_{max} = 18.92$. The time step is $\Delta t = 5 \times 10^{-4}$ and the plane-averaged turbulence statistics values are gathered from $t^+ = 60$ to $t^+ = 80$.

Jarrin [33] and Okong'o et al. [34] are chosen as references, in which LES has been used in an unstructured grid. Fig. 18 shows the planar average of time-averaged velocity, normalized by the friction velocity. The experimental log-law from Eckelmann [35] is $u^+ = 2.65 \text{ In}(z^+) + 5.9$ for a nearby friction Reynolds number cases. Obviously, LES result in this paper using coarse mesh has excellent agreement with experimental data of Eckelmann [35] and numerical data from Okong'o et al. and Jarrin. Using fine mesh, LES result is close to numerical results of Jarrin [33] with the same mesh, the predicted velocities from both are very slightly higher than the log law $u^+ = 2.5\ \mathrm{In}(z^+) + 5.5$ given by Kim et al. [30] using DNS. A discrepancy of about 6% between DNS and Experimental results from Eckelmann [35] has been observed. The explanation about this discrepancy can be found in Kim et al. [30].

The computed streamwise turbulent intensity (u_{rms}, v_{rms}, w_{rms}, where the subscript rms stands for root mean squared) and Reynolds stress using two meshes are shown in Fig. 19. The tendency of current results is in good agreement with the reference data, with a very slight difference of the turbulent intensity, compared with the references in streamwise direction. Results in the current study exhibit increased turbulence generation in the buffer region, which leads to a higher turbulence intensity and a higher mean velocity profile. Using the iso-surface Q-criterion of instantaneous flow in the lower half channel, Fig. 20 shows the hairpin structures, which are randomly distributed over the turbulent flow field and an instantaneous velocity profile in the full channel.

6.3. Lid-driven cavity flow

Many researchers have investigated the lid-driven cavity flow test-case using either simulations or experiments since the work by Ghia et al. [36]. The typical computational domain for this problem is a cubic domain. On the top, a uniform constant horizontal velocity is imposed, serving as the moving lid that drives the flow. The rest are set as no-slip boundaries. Two sets of boundary conditions are proposed for this problem: first, periodic boundary condition in the spanwise (y) direction, representing a 2D problem [37]; and second wall boundary condition in the spanwise (y) direction, representing a fully 3D problem. Here, simulations are conducted in low and moderate Reynolds number ($Re = 100$, 400, 1000) using DNS or LES as Bouffanais et al. [37]. For low Reynolds number cases ($Re = 100$, 400), the domain is discretized using a structured right-angled grid resolution of $N_x = 32$ and $N_z = 64$ uniform vertical layers. A refined mesh in the corner in the $x - y$ plane is used for $Re = 1000$ to capture the secondary vortex. Uniform vertical layers are used for all these tests.

6.3.1. Low Reynolds number

The velocity profiles at the horizontal and vertical midsections for both 2D and 3D problem at low Reynolds numbers are shown in Fig. 21 and Fig. 22. The results of Ghia et al. [36] with fine grid configuration is plotted for comparison. For 2D simulation, fair agreement with the reference data is observed. Close to the top boundary, the gradient of the streamwise velocity is relatively small, which means a very weak shear stress here. As the flow moves close to the center, the streamwise velocity drops rapidly, indicating the presence of a vortex structure and reverse pressure gradient. Close to the bottom wall, a nearly parabolic distribution of the streamwise velocity is observed, implying that the shear stress is the dominating factor to sustain this velocity field. For the vertical midsection velocity distribution, a nearly symmetry profile and mild velocity gradient are observed from the left wall to the right wall, indicating the vertical midsection is not greatly disturbed by the vortex structure at the top but mostly affected by the confinement of the side walls.

For 3D simulation, as no direct reference data is available, another finite-volume method based code CgLES [38, 39] was applied for validation at $Re = 400$. The simulations by CgLES are run under the same geometry and boundary conditions, but with much finer grid resolution ($N = 256$). The results obtained from our code and the reference code are almost identical and are different from the 2D results, which means that the boundary wall affects the flow field and makes the problem fully three-dimensional.

6.3.2. Moderate Reynolds number

The steady state on a vertical plane ($y = 0.5$) at $Re = 1000$ is presented in Fig. 23. Note that driven by the top lid, the velocity field forms a rotational pattern with a main vortex slightly shifting into the top right section and a pair of secondary vortex near the bottom corners. From the top wall to the vortex center, the streamwise velocity gradually decreases and becomes negative as it moves away from the vortex center towards the bottom wall. The highest vertical velocity is observed to be near the top-left and top-right corner, indicating a change of flow direction due to the confinement of the side walls. The velocity profile agrees very well with the results of Tang et al. [40].

6.4. Flow over a static vertical cylinder

The flows around a circular cylinder is another well-known benchmark problem for validating external flows [9]. At lower Reynolds number ($Re_D < 47$), where D is the diameter of the cylinder, the flow will form a stable re-circulation bubble behind the cylinder. If Re_D increases up to 200, then a stable vortex shedding is formed and the flow remains two-dimensional. For $Re_D > 1000$, flows become fully three-dimensional.

6.4.1. Low Reynolds number

Here we present the results of computing flows using the direct numerical simulations at Reynolds numbers from 50 to 200, where the flow shows 2D properties. The non-dimensional diameter of the cylinder $D = 1$. The computational domain is set as $[-10, 20] \times [-15, 15] \times [0, 1.12]$ in the streamwise, spanwise, and vertical direction, respectively. A uniform inflow boundary condition is imposed at the inlet with a non-dimensional unit velocity. In the spanwise direction, free slip boundary condition is used to minimize the effect of wall boundaries. In the vertical direction, periodic boundary condition is used to mimic an infinite long cylinder. The computational domain in $x - y$ direction is about $20,000$ triangular elements (unstructured) with 20 vertical layers. To ensure the first layer points lie within the boundary layer, 157 mesh points are constructed around the cylinder and the distance from the first layer cell centers to the wall is about $\delta = 0.01$. In the numerical study presented by Qu et al. [41], a similar rectangle size was employed, but with a closer distance from the wall to the first grid point ($\delta = 0.005$). All the simulations are initially performed for 100 time units (D/U) until the solution is statistically stable and then the simulation is restarted for another 300 time units to gather the time averaged data.

The evolution of the recirculation length as a function of the Reynolds numbers is shown in Fig. 24. From the time averaged statistics, it can be seen that the length of the recirculation area moves towards the cylinder body as the Reynolds number increases. Note that the recirculation-area length is close to the experimental measurements of Nishioka and Sato [42] and the computational results of Park et al.[43]. Last one considers a fine grid resolution of 641×241 points. A fair agreement is found between the current result and the reference data.

Results on drag and lift coefficients are shown in Table 8. The values C_d andC_l are the drag and lift coefficients, respectively. It is composed for the mean value and maximum deviation from averaging in time. Note that the mean drag coefficients decrease as Reynolds number increases, meanwhile the oscillation amplitude increases continuously. Quantitatively, the proposed method tends to over-predict the values as compared with other numerical results, especially from Qu et al.[41] data for low Reynolds numbers. This deviation can be explained due to the difference in the size of computational domain, spatial or temporal resolution, and boundary conditions.

Table 8: Drag and lift coefficients for unsteady flow past a cylinder at various Reynolds number.

	Current results		Park et al. [43]		Mittal et al. [44]	Qu et al. [41]
Re_D	C_d	C_l	C_d	C_l	C_d	C_d
50	1.476±0.005	±0.062	—	—	1.416	1.397
60	1.432±0.006	±0.146	1.39	±0.1344	—	1.377
80	1.389±0.007	±0.340	1.35	±0.2452	—	1.336
100	1.374±0.044	±0.341	1.33	±0.3321	1.322	1.317
120	1.361±0.018	±0.420	1.32	±0.4103	—	1.306
150	1.357±0.028	±0.526	—	—	—	1.305
200	1.347±0.045	±0.673	—	—	1.327	1.316

6.4.2. Moderate Reynolds number

As a demonstration of the capacity of the numerical model, we simulate turbulent flows around a cylinder. It represents a complex phenomenon in computational fluid dynamics and a challenging test case for all 3D Navier-Stokes solvers. The phenomenon of horseshoe vortex (HV) oscillation has been intensively studied by many researchers both experimentally and computationally, and can serve as a reference for the current test case.

In this section, large eddy simulation is performed using $Re_D = 4460$ for a systematic study of the 3D horseshoe vortex and the wake behind the cylinder. The inflow velocity is given by a Poiseuille profile with the mean value as unit velocity; and the inflow boundary layer thickness is $\delta/D = 0.59D$. In the vertical boundaries, the bottom is set a no-slip wall and the top is set as a free slip wall. A fine grid resolution in both horizontal and vertical directions is employed. The number of cells in the horizontal domain is about $41,202$ with 424 points along the cylinder surface. The first row of cells is situated at $0.003D$ away from the cylinder surface, corresponding to 0.75 wall units. In this simulation, 128 vertical layers with finer resolution close to the bottom are employed to capture the oblique pattern of vortex shedding.

The adverse pressure gradients induced by the cylinder obstruction create downflows in front of the cylinder, and generate horseshoes system near the bottom and a wake region behind the cylinder. Fig. 25 (a) shows the main coherent structures in an instantaneous flow associated to a HV system on a rigid bed using the Q criterion. Three non-dimensional vortices (Developing Vortex - DV1, Primary Vortex - PV1, Corner Vortex - CV1) and two counter-rotating Bottom-Attached Vortices (BAV1 and BAV2) are clearly observed. As Kirkil et al. [45], this figure illustrates the development of smaller-scale instabilities along the legs of BAV2. Fig. 25(b) presents 3D streamlines, which clearly illustrates the HV system around the cylinder. Thanks to the use of a fine-mesh resolution, numerical results can show rotational movements of HV around themselves.

To demonstrate the behavior of the numerical method during the time evolution, we plot the streamlines of the flow in front of the cylinder on a vertical plane (at the central axis). Fig. 26 (a) shows 14 time stages during an oscillating cycle of the HV system. There are three primary clockwise vortices (PV) close to the bottom, forming a necklace vortex system. As reported by Kirkil and Constantinescu [46], a typical horseshoe vortex system can consist of six individual vortices and its dynamic depends largely on the Reynolds number and on the characteristics of the incoming boundary layer. According to the smoke tunnel study by Baker [47], it is expected that counter-clockwise vortex should exist in the adjoining region between the cylinder and the bottom to each of the main vortex.

The structure of the computed HV system is also compared with one observed in an experiment conducted at $Re_D = 2250$ by Lin et al. [48], as illustrated in Fig. 26(b). The HV system is in the breakaway sub-regime. Note that a nearly perfect agreement on HV system pattern has been obtained. Three main vortexes are correspondingly: DV1 located at the upstream side from the cylinder, PV1 at the middle, and CV1 at the closest position to the cylinder. The overall process behaves as follows. First, DV1 is formed upstream among these three vortices, it originates from the position where the separated boundary layer starts to evolve, and moves downstream to become a new Primary Vortex (PV2). Subsequently, as the PV1 moves closer to the juncture of the cylinder, it becomes a new Corner Vortex (CV2). The similar expression of HV system is due to the similar relative thickness of the incoming boundary layer and similar Reynolds number.

7. Code performance

An efficient solution of the N-S equation is fundamental to the successful development of the proposed three-dimensional nonhydrostatic model for the turbulent flows. In this paper, we employ an explicit formulation based on the Adams-Bashforth scheme. In terms of performance, an implicit time-stepping approach may reduce the simulation time by taking larger values of the time step; however, additional linear system needs to be solved. In a recent publication [26], the authors have proposed a second-order time implicit formulation for a free-surface code allowing us to obtain more stable and accurate solutions for large time step Δt. However, the most time-consuming part of the code is still the solution of the pressure Poisson equation (28).

In this section, the convergence of the BICGSTAB method is analyzed. First, the performance of the Poison problem is tested over a rectangular domain with structured right-angled grids. Next, we investigate the number of iteration and CPU time of simulations using the test case of lid-driven cavity flow. We report the results of this section on a standard twenty-core 3.0 GHz Intel Xeon. All of our codes are implemented in FORTRAN language.

The number of iterations of the BICGSTAB solver as a function of the tolerance value is studied in Fig. 27 . Structured equilateral and unstructured grids are used with resolutions $N = 16$, 32 and 64 in all directions. In the same figure, we plot the L_∞-norm error between the numerical and the analytical solution of the finite volume discretization. Note that the residual of the BICGSTAB solver reaches its minimum discretization error for a tolerance value close to $\epsilon = 0.5\Delta x^2$. It means that there in not improvement using a lower tolerance value. The same behavior is obtained using the L_2-norm (results are not shown here). Thus, the solver takes only few number of iterations to converge to the solution: 19, 48 and 107 iterations for $N = 16$, 32 and 64, respectively. These numbers can be lower by taking the solution of the previous time step in the N-S simulations, as we described in the following section. The corresponding CPU time is displayed in Table 9. We remark that the unstructured grid converges similar as the structured one for this test case. This can be explained because both connectivity matrices for the full 3D discretization are similar. The vertical layers indexation employed for both cases is the same.

Table 9: Performance of the BICGSTAB method for the 3D Poisson problem using different grid resolutions.

		Structured			Unstructured		
N	$\Delta t = 0.5\Delta x^2$	Elements	Iterations	CPU time	Elements	Iterations	CPU time
16	8.8×10^{-3}	6750	19	0.04 sec	6750	22	0.05 sec
32	2.0×10^{-3}	59582	48	0.94 sec	69254	49	1.03 sec
64	5.0×10^{-4}	500094	107	15.49 sec	581112	98	14.99 sec

Now, we investigate the performance of BICGSTAB solver during the time simulation. The simulation from $t = 0$ to $t = 20$ for the lid-driven cavity flow problem with $Re = 100$ was selected for this test. The domain is discretized using a structured right-angled grid resolution of $N_x = 32$ and $N_z = 20$ uniform vertical layers. The time step was set as $\Delta t = 2 \times 10^{-3}$. Fig. 28 shows the number of iterations, CPU time and final residual to satisfied a tolerance value of $\epsilon = 10^{-7}$. Few iterations are required for this problem even a small tolerance value was selected. Note that the number of iterations reduces until only one iteration is required when the problem already reached its steady state. Each iteration takes around 0.018 seconds.

The total CPU time required for this sequential simulation was around 30 minutes. For fine resolution test cases, a parallel code is necessary due to the large amount of data that the 3D problem produces. We must be careful to consider proper parallel techniques in order to achieve a good performance. An analysis in this direction will be studied in a future work.

8. Conclusions

In this paper, a novel numerical solver has been developed for modeling nonhydrostatic turbulent flows using an unstructured finite-volume method with large eddy simulation. The approximation of values and outward-normal derivative at the cell face in the discretization equation is presented. This approximation will have a direct impact on the accuracy in space of the proposed numerical model. A filtering technique used in the Momentum Interpolation Method avoids the triangular C-grid divergence noise problem for both structured and unstructured grids. An increase of accuracy is observed with the cross diffusion in the outward-normal face derivatives terms in the 3D pressure Poisson equation. In this case, we also notice that the horizontal approximations dominates the global accuracy for grid aspect ratio $R \approx 1$ and the numerical solution is still accurate for grid aspect ratio $R \gg 1$. The advection problem verified the proposed central scheme and the 2D decaying vortex test demonstrates that the proposed method is second-order accuracy in space and time, which allows simulations of nonhydrostatic flows at the moderate Reynolds numbers. Several test cases have been used to check the ability of the proposed model to accurately simulate laminar and turbulent flows. Fair agreements with previous studies have been obtained by backward-facing step flow, the lid-driven cavity flow and the turbulent channel flows simulated by DNS and LES. In the test case of flows around a vertical cylinder, the time averaged pressure coefficient for 2D problem and horseshoe vortex oscillation for 3D problem at moderate Reynolds number have been compared with previous experimental and numerical studies. Coherent structure of flows has been shown. Furthermore, performance analysis of the code has been included in the paper. Clearly, the proposed projection method with a combination of Momentum Interpolation Method and a central scheme has been proved to be robust, accurate and reliable for further researches.

Acknowledgments

The authors gratefully acknowledge the INRS-SINAPSE project (ComputeCanada No. 2871), the Mexican Council of Science and Technology project (CONACYT No. 256252) and the Chinese Scholarship Council (CSC) for their financial supports to do this work. The authors extend special thanks to Électricité de France Recherche & Development (EDF R&D) for their support in providing the access to the computing facility.

References

[1] W. Wu, Depth-averaged two-dimensional numerical modeling of unsteady flow and non-uniform sediment transport in open channels, Journal of Hydraulic Engineering, vol. 130, no. 10, pp. 1013-1024, 2004.

[2] Z. Horvat, M. Isic, and M. Spasojevic, Two dimensional river flow and sediment transport model, Environmental Fluid Mechanics, vol. 15, no. 3, pp. 595-625, 2015.

[3] H. Zhu, L. Wang, and H. Tang, Large-eddy simulation of suspended sediment transport in turbulent channel flow, Journal of Hydrodynamics, vol. 25, no. 1, pp. 48-55, 2013.

[4] T. C. Huang, C. Y. Chang, and C. A. Lin, Simulation of droplet dynamic with high density ratio two-phase lattice Boltzmann model on multi-GPU cluster, Computers & Fluids, vol. 173, pp. 80-87, 2018.

[5] R. Steijl and G. N. Barakos, Parallel evaluation of quantum algorithms for computational fluid dynamics, Computers & Fluids, vol. 173, pp. 22-28, 2018.

[6] F. Capuano, A. Mastellone, and E. M. De Angelis, A conservative overlap method for multi-block parallelization of compact finite-volume schemes, Computers & Fluids, vol. 159, pp. 327-337, 2017.

[7] C. M. Rhie and W. L. Chow, Numerical study of the turbulent flow past an airfoil with trailing edge separation, AIAA Journal, vol. 21, no. 11, pp. 1525-1532, 1983.

[8] Y. Zang, R. L. Street, and J. R. Koseff, A non-staggered grid, fractional step method for time-dependent incompressible Navier-Stokes equations in curvilinear coordinates, Journal of Computational Physics, vol. 114, no. 1, pp. 18-33, 1994.

[9] D. Kim and H. Choi, A second-order time-accurate finite volume method for unsteady incompressible flow on hybrid unstructured grids, Journal of Computational Physics, vol. 162, no. 2, pp. 411-428, 2000.

[10] Y. J. Jan and T. W. H. Sheu, A quasi-implicit time advancing scheme for unsteady incompressible ?ow. Part I: Validation, Comput. Methods Appl. Mech. Engrg., vol. 196, no. 45-48, 4755-4770, 2007.

[11] A. Dalal, V. Eswaran, and G. Biswas, A Finite-Volume method for Navier-Stokes equations on unstructured meshes, Numerical Heat Transfer, Part B: Fundamentals, vol. 54, no. 3, pp. 238-259, 2008.

[12] S. J. Liang, Y. J. Jan, and C. A. Huang, A quasi-Implicit time-advancing scheme for flow in a three-dimensional curved duct, Numerical Heat Transfer, Part B: Fundamentals, vol. 64, no. 4, pp. 306-325, 2013.

[13] K. Mahesh, G. Constantinescu, and P. Moin, A numerical method for large-eddy simulation in complex geometries, Journal of Computational Physics, vol. 197, no. 1, pp. 215-240, 2004.

[14] K. Mahesh, G. Constantinescu, S. Apte, G. Iaccarino, F. Ham, and P. Moin, Large-Eddy simulation of reacting turbulent flows in complex geometries, Journal of Applied Mechanics, vol. 73, no. 3, pp. 374-381, 2006.

[15] L. Davidson, A pressure correction method for unstructured meshes with arbitrary control volumes, International Journal for Numerical Methods in Fluids, vol. 22, no. 4, pp. 265-281, 1996.

[16] F. Ducros, F. Laporte, T. Souléres, V. Guinot, P. Moinat, and B. Caruelle, High-order fluxes for conservative skew-symmetric-like schemes in structured meshes: Application to Compressible Flows, Journal of Computational Physics, vol. 161, no. 1, pp. 114-139, 2000.

[17] P. J. Mason and D. J. Thomson, Stochastic backscatter in large-eddy simulations of boundary layers, J. Fluid Mech., vol. 242, no. 1, pp. 51-78, 1992.

[18] J. W. Deardorff, A numerical study of three-dimensional turbulent channel flow at large Reynolds numbers, Journal of Fluid Mechanics, vol. 41, no. 2, pp. 453-480, 1970.

[19] O. B. Fringer, M. Gerritsen, and R. l. Street, An unstructured-grid, finite-volume, nonhydrostatic, parallel coastal ocean simulator, Ocean Modelling, vol. 14, no. 3, pp. 139–173. 2006.

[20] J. A. Jankowski, Parallel implementation of a non-hydrostatic model for free surface flows with semi-Lagrangian advection treatment. International journal for numerical methods in fluids, vol. 59, no. 10, pp. 1157-1179. 2009.

[21] A. J. Chorin, Numerical solution of the Navier-Stokes equations, Mathematics of Computation, vol. 22, no. 104, pp. 745-762, 1968.

[22] S. C. Xue and G. W. Barton, A finite volume formulation for transient convection and diffusion equations with unstructured distorted grids and its applications in fluid flow simulations with a collocated variable arrangement, Computer Methods in Applied Mechanics and Engineering, vol. 253, pp. 146-159, 2013.

[23] H. Wan, et al., The ICON-1.2 hydrostatic atmospheric dynamical core on triangular grids, Part I: formulation and performance of the baseline version. Geoscientific Model Development, vol. 6, pp. 735-763. 2013.

[24] P. J. Wolfram and O. B. Fringer, Mitigating horizontal divergence checker-board oscillations on unstructured triangular C-grids for nonlinear hydrostatic and nonhydrostatic flows. Ocean Modelling, vol. 69, pp. 64-78. 2013.

[25] B. Perot, Conservation properties of unstructured staggered mesh schemes. Journal of Computational Physics vol. 159, pp. 58-89. 2000.

[26] M. Uh Zapata, W. Zhang, D. Pham Van Bang and K. D. Nguyen, A parallel second-order unstructured finite volume method for 3D free-surface flows using a σ-coordinate, Computers & Fluids, vol. 190, pp. 15-29, 2019.

[27] D. Vidović, A. Segal, & P. Wesseling, A superlinearly convergent Mach-uniform finite volume method for the Euler equations on staggered unstructured grids. J. Comp. Physics, vol. 217, no. 2, pp. 277-294. 2006.

[28] A. Shapiro, The use of an exact solution of the Navier-Stokes equations in a validation test of a three-dimensional nonhydrostatic numerical models. Monthly Weather Review, vol. 121, pp. 2420-2425. 1993.

[29] B. F. Armaly, F. Durst, J. C. F. Pereira, and B. Schönung, Experimental and theoretical investigation of backward-facing step flow, J. Fluid Mech., vol. 127, no. 1, pp. 473-496, 1983.

[30] J. Kim, P. Moin, and R. Moser, Turbulence statistics in fully developed channel flow at low Reynolds number, Journal of Fluid Mechanics, vol. 177, no. 1, pp. 133-166, 1987.

[31] T. Lee and D. Mateescu, Experimental and numerical investigation of 2D backward-facing step flow, Journal of Fluids and Structures, vol. 12, no. 6, pp. 703-716, 1998.

[32] P. T. Williams and A. J. Baker, Numerical simulations of laminar flow over a 3D backward-facing step, International Journal for Numerical Methods in Fluids, vol. 24, no. 11, pp. 1159-1183, 1997.

[33] N. Jarrin, Synthetic inflow boundary conditions for the numerical simulation of turbulence, University of Manchester, 2008.

[34] N. Okong'O, D. D. Knight, and G. Zhou, Large Eddy Simulations using an unstructured grid compressible Navier-Stokes algorithm, International Journal of Computational Fluid Dynamics, vol. 13, no. 4, pp. 303-326, 2000.

[35] H. Eckelmann, The structure of the viscous sublayer and the adjacent wall region in a turbulent channel flow, Journal of Fluid Mechanics, vol. 65, no. 3, pp. 439-459, 1974.

[36] U. Ghia, K. N. Ghia, and C. T. Shin, High-Re solutions for incompressible flow using the Navier-Stokes equations and a multigrid method, Journal of Computational Physics, vol. 48, no. 3, pp. 387-411, 1982.

[37] R. Bouffanais, M. O. Deville, and E. Leriche, Large-eddy simulation of the flow in a lid-driven cubical cavity, Physics of Fluids, vol. 19, no. 5, p. 055108, 2007.

[38] T. G. Thomas and J. J. R. Williams, Turbulent simulation of open channel flow at low Reynolds number, International Journal of Heat and Mass Transfer, vol. 38, no. 2, pp. 259-266, 1995.

[39] C. Ji, A. Munjiza, and J. J. R. Williams, A novel iterative direct-forcing immersed boundary method and its finite volume applications, Journal of Computational Physics, vol. 231, no. 4, pp. 1797-1821, 2012.

[40] L. Q. Tang, T. Cheng, and T. T. H. Tsang, Transient solutions for three-dimensional lid-driven cavity flows by a least-squares finite element method, International Journal for Numerical Methods in Fluids, vol. 21, no. 5, pp. 413-432, 1995.

[41] L. Qu, C. Norberg, L. Davidson, S. H. Peng, and F. Wang, Quantitative numerical analysis of flow past a circular cylinder at Reynolds number between 50 and 200, Journal of Fluids and Structures, vol. 39, pp. 347-370, 2013.

[42] M. Nishioka and H. Sato, Measurements of velocity distributions in the wake of a circular cylinder at low Reynolds numbers, Journal of Fluid Mechanics, vol. 65, no. 1, pp. 97-112, 1974.

[43] J. Park, K. Kwon, and H. Choi, Numerical solutions of flow past a circular cylinder at Reynolds numbers up to 160, KSME International Journal, vol. 12, no. 6, pp. 1200-1205, 1998.

[44] S. Mittal and A. Raghuvanshi, Control of vortex shedding behind circular cylinder for flows at low Reynolds numbers, International journal for numerical methods in fluids, p. 421-447. 2001.

[45] G. Kirkil and G. Constantinescu, Flow and turbulence structure around an in-stream rectangular cylinder with scour hole: flow around a rectangular cylinder, Water Resources Research, vol. 46, no. 11, 2010.

[46] G. Kirkil and G. Constantinescu, A numerical study of the laminar necklace vortex system and its effect on the wake for a circular cylinder, Physics of Fluids, vol. 24, no. 7, p. 073602, 2012.

[47] C. J. Baker, The laminar horseshoe vortex, Journal of Fluid Mechanics, vol. 95, no. 2, pp. 347-367, 1979.

[48] C. Lin, W. J. Lai, and K. A. Chang, Simultaneous particle image velocimetry and laser doppler velocimetry measurements of periodical oscillatory horseshoe vortex system near square cylinder-base plate juncture, Journal of Engineering Mechanics, vol. 129, no. 10, pp. 1173-1188, 2003.

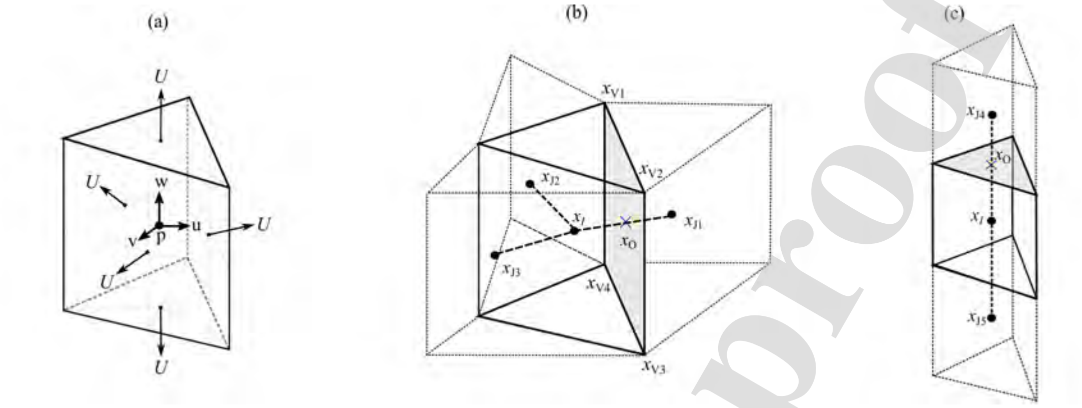

Figure 1: (a) 3D schematic variables stored in the cell-centers for the non-staggered grid. Sketch of geometry entities of the (b) horizontal and (c) vertical neighbor elements.

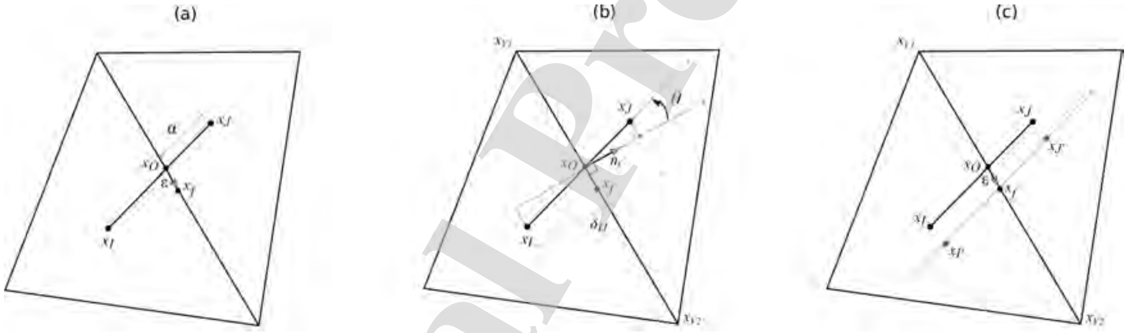

Figure 2: Interpolation of flow variables at the mid-point on the cell face for the (a) convective and (b)-(c) diffusive terms.

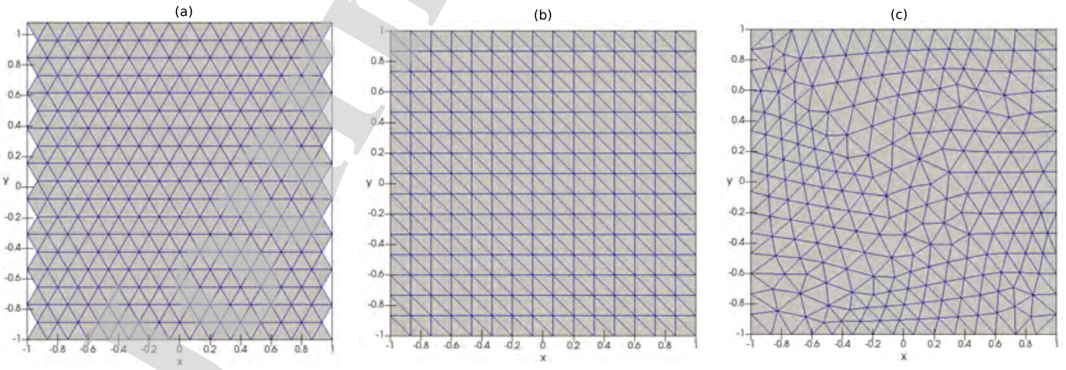

Figure 3: Types of triangular grids: (a) structured equilateral grid, (b) structured right-angled grid, and (b) unstructured grid.

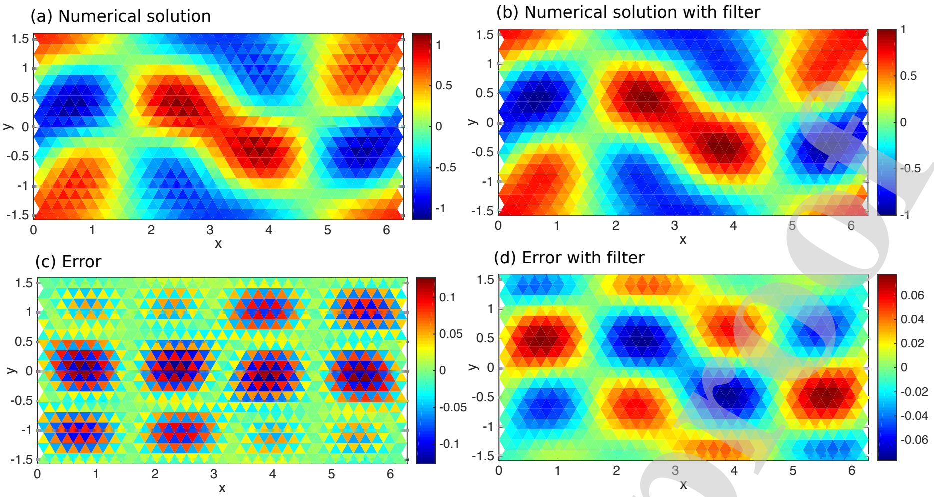

Figure 4: Numerical solution and error of the divergence of the velocity field calculated using an equilateral triangular grid with $\Delta x = 0.2$ resolution. The solution is calculated without and with the filter technique.

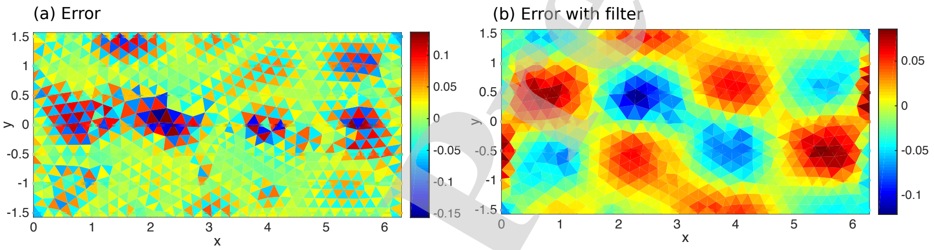

Figure 5: Error of the divergence of the velocity field using an unstructured grid without and with the filter technique.

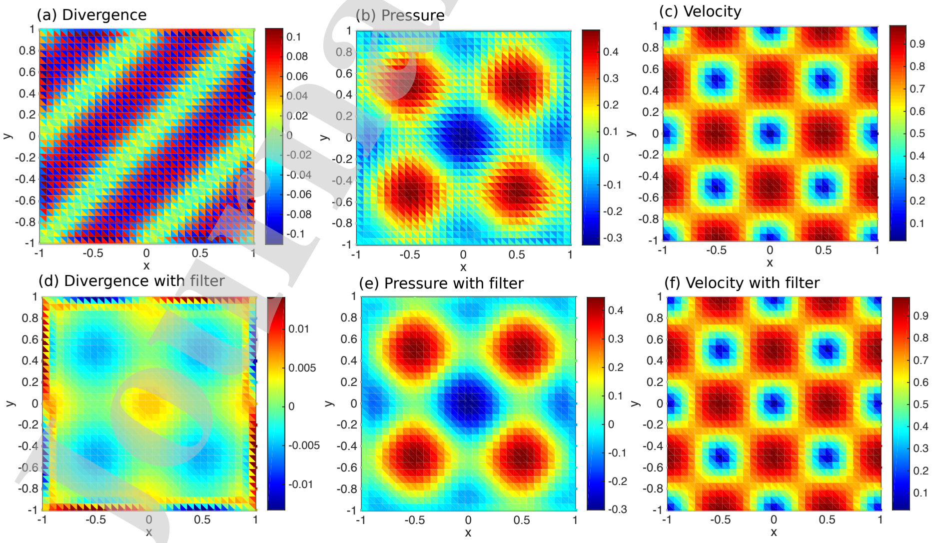

Figure 6: Numerical solution of the divergence of the intermediate velocity field, pressure and velocity magnitude for the 2D Taylor Vortex problem. The solution is calculated using a right-angled triangular grid without and with the filter technique.

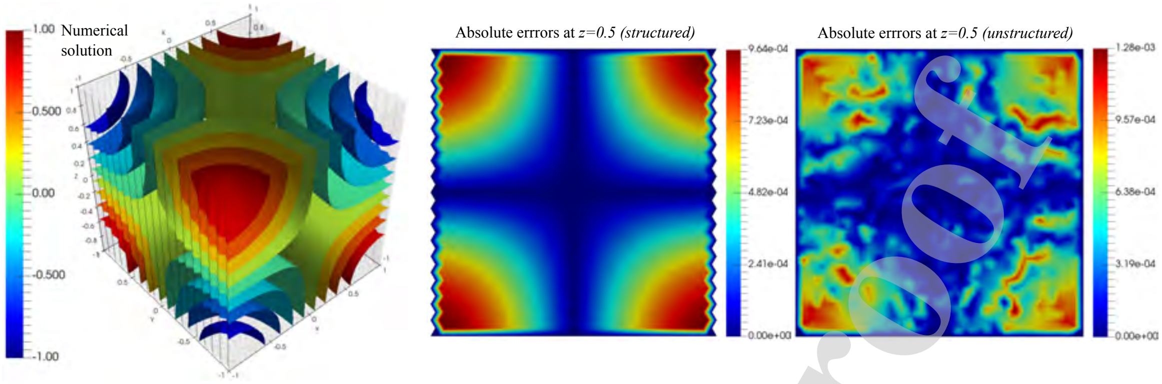

Figure 7: Numerical solution and absolute errors for the 3D Poisson equation at $z = 1/2$ using $N = 32$ for structured and unstructured grids.

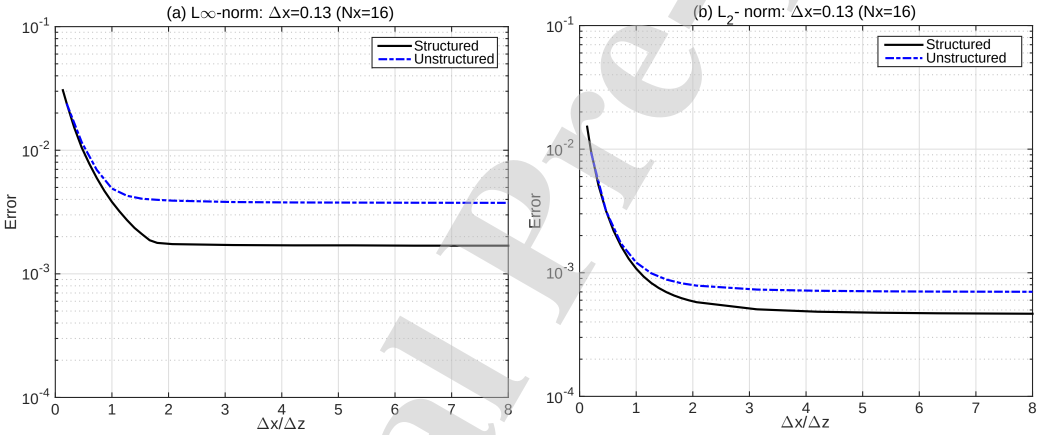

Figure 8: Norm errors for the 3D Poisson equation using different number of layers in the vertical direction.

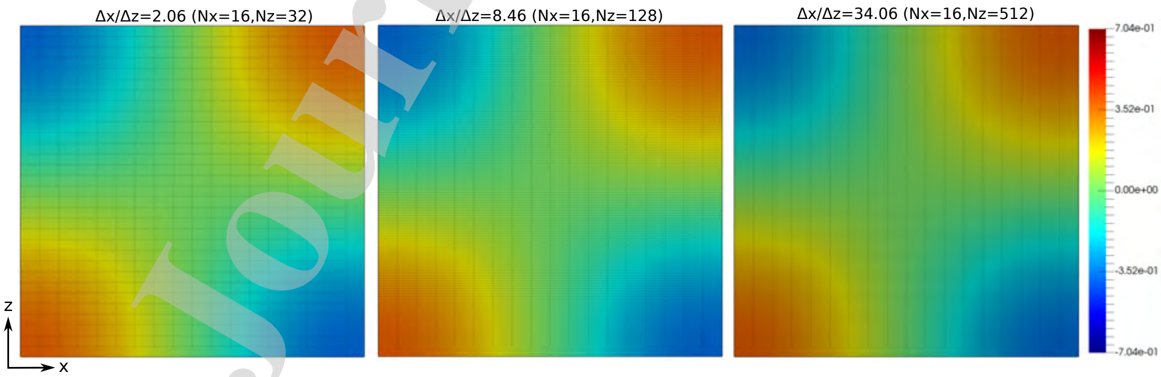

Figure 9: Numerical solution for the 3D Poisson equation at $y = 0.25$ varying the number of vertical layers.

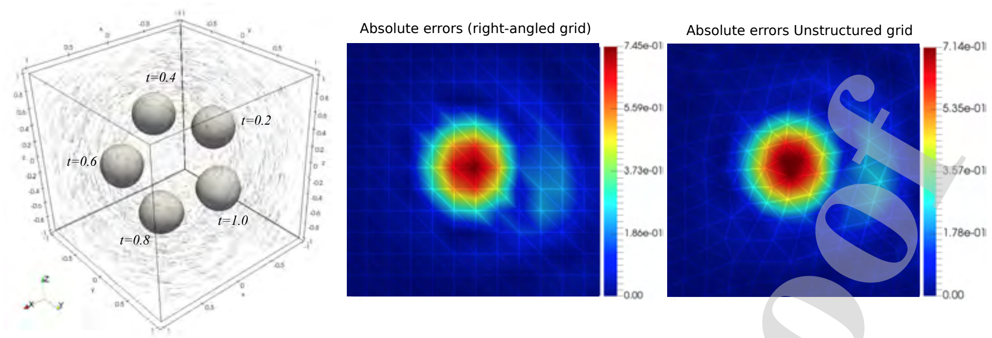

Figure 10: Numerical solution of the 3D cosine bell example at different time stages (left), and absolute errors at $z = -1/(2\sqrt{2})$ and $T = 1$.

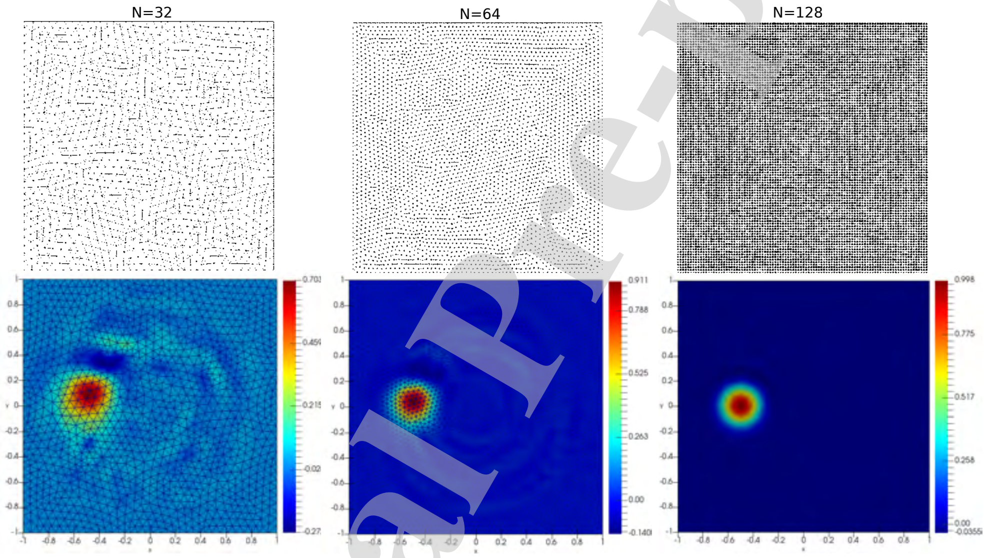

Figure 11: Numerical solution of the 2D cosine bell example using different unstructured grids.

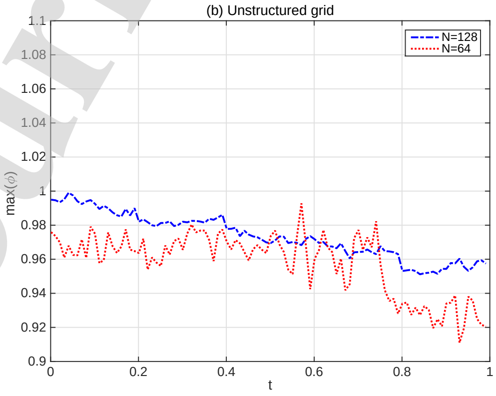

Figure 12: Peak values of the 2D advection equation using unstructured grids.

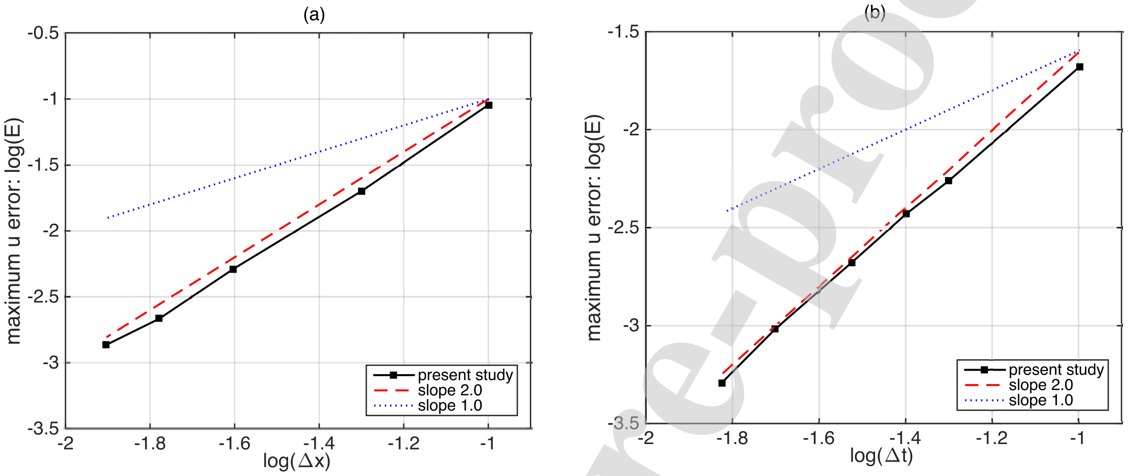

Figure 13: Convergence analysis of the (a) spatial and (b) temporal discretization. The slopes show the positions of first and second order of accuracy.

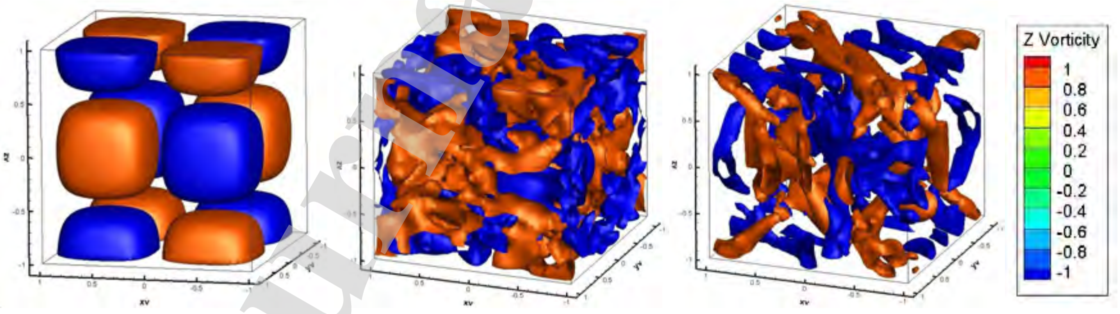

t=0 t=5 t=10

Figure 14: Iso-surfaces of the z-component of vorticity at different time stages for the decaying vortex problem using $Re = 1600$.

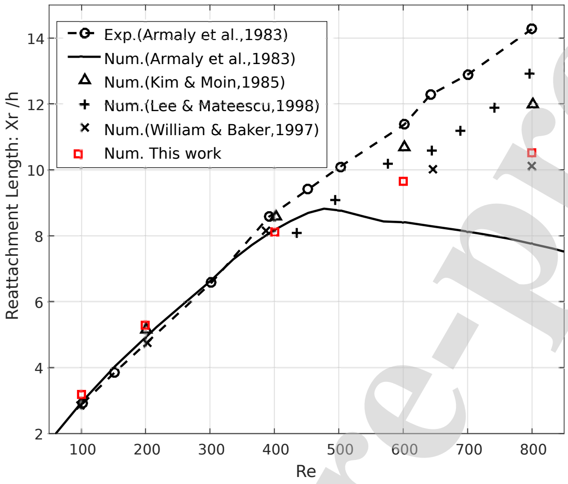

Figure 15: 2D simulation of reattachment length as a function of the Reynolds number.

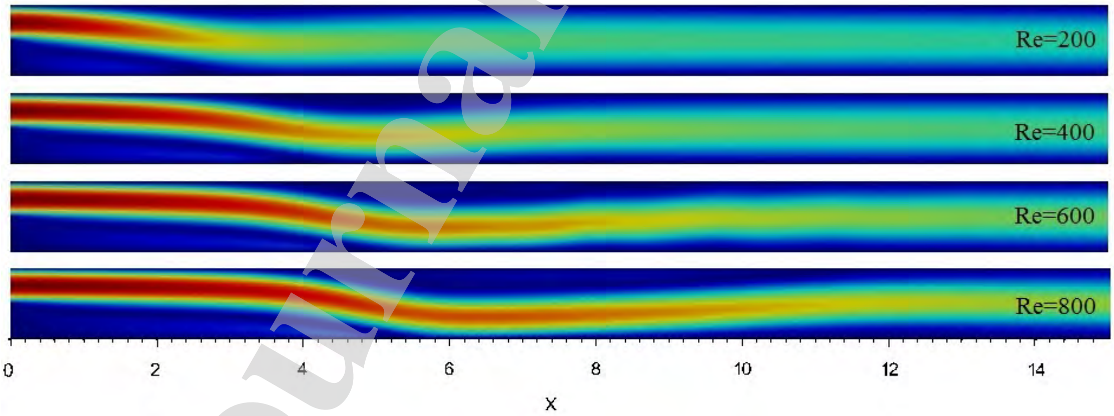

Figure 16: Visualization of the steady 2D base flows at different Reynolds number.

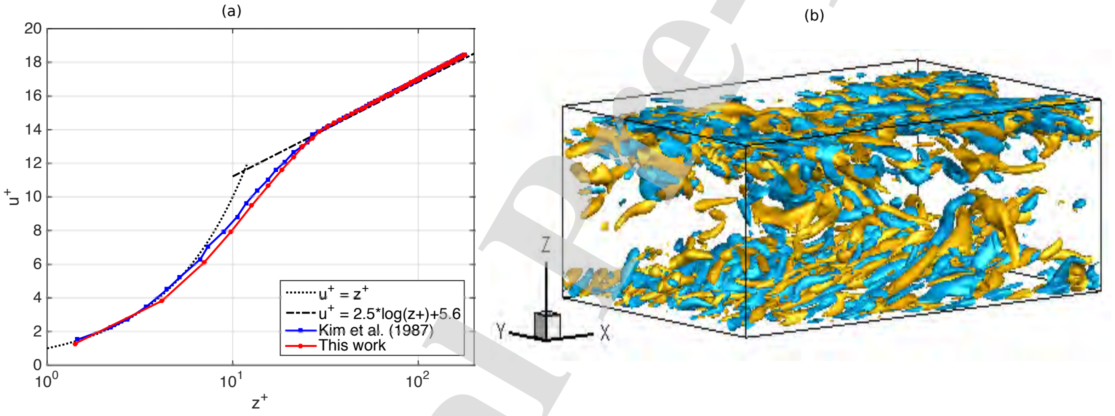

Figure 17: (a) Iso-surface of Q-criterion field showing direct simulation of turbulent structure in the open channel flows. (b) Mean streamwise velocity distribution in wall units by direct numerical simulation.

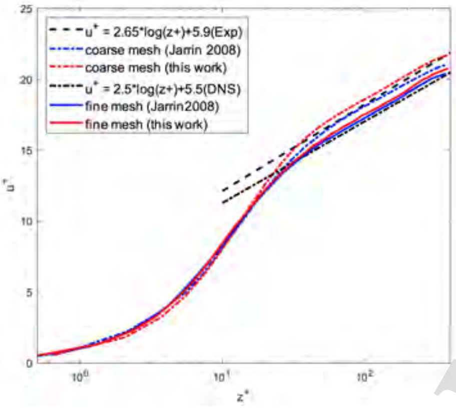

Figure 18: Large eddy simulation of mean streamwise velocity distribution in wall units.

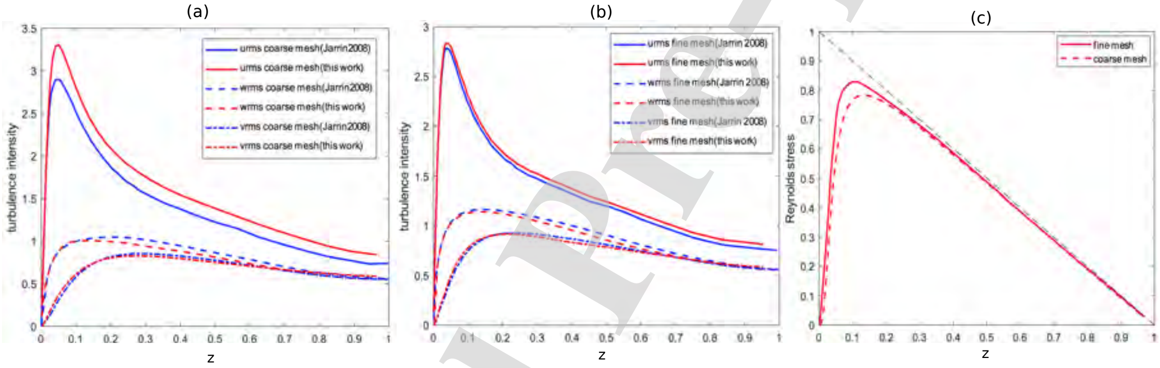

Figure 19: Large eddy simulation of the turbulent channel flow: (a) Streamwise turbulence intensity using coarse mesh (b) Streamwise turbulence intensity using coarse mesh and (c) Reynolds stress.

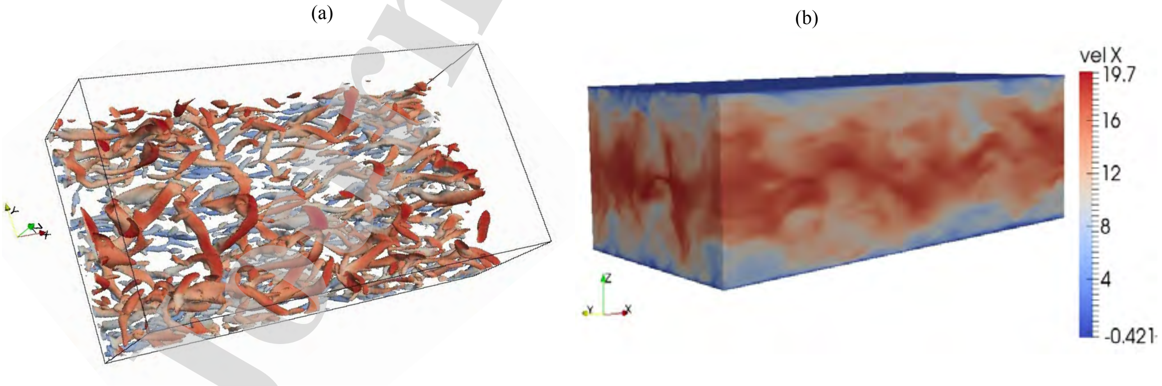

Figure 20: Large eddy simulation of of the turbulent channel flow: (a) Iso-surface of Q-criterion field showing turbulent structure and (b) Instantaneous velocity profile.

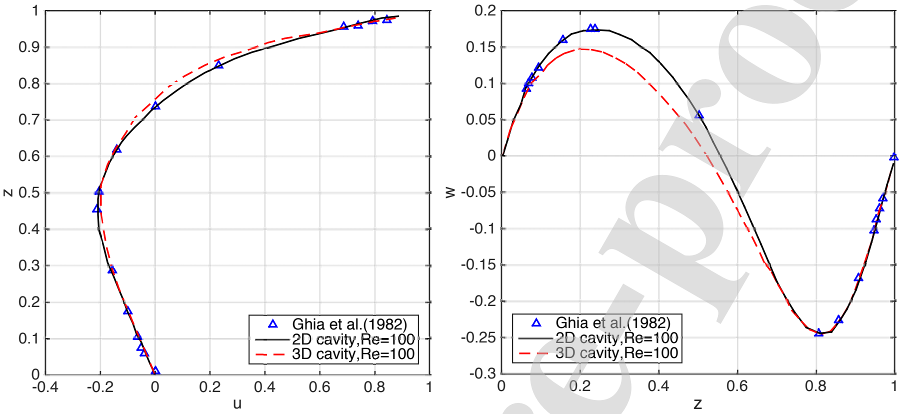

Figure 21: Profile of horizontal midsection velocity (u) and vertical midsection velocity (w) at $Re = 100$.

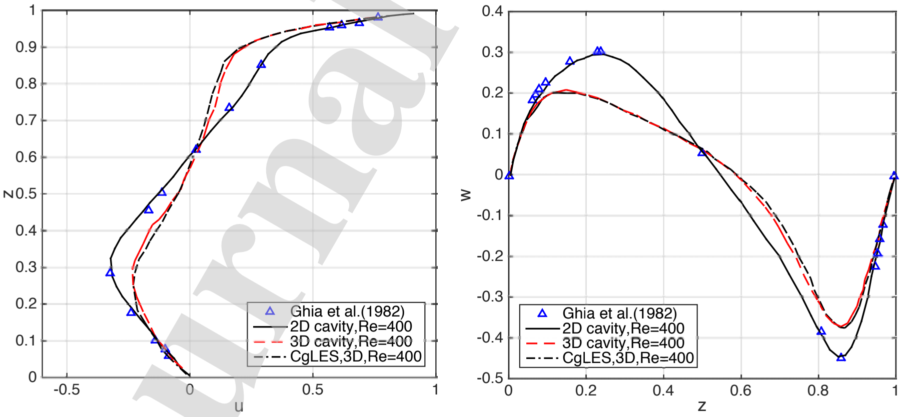

Figure 22: Profile of horizontal midsection velocity (u) and vertical midsection velocity (w) at $Re = 400$.

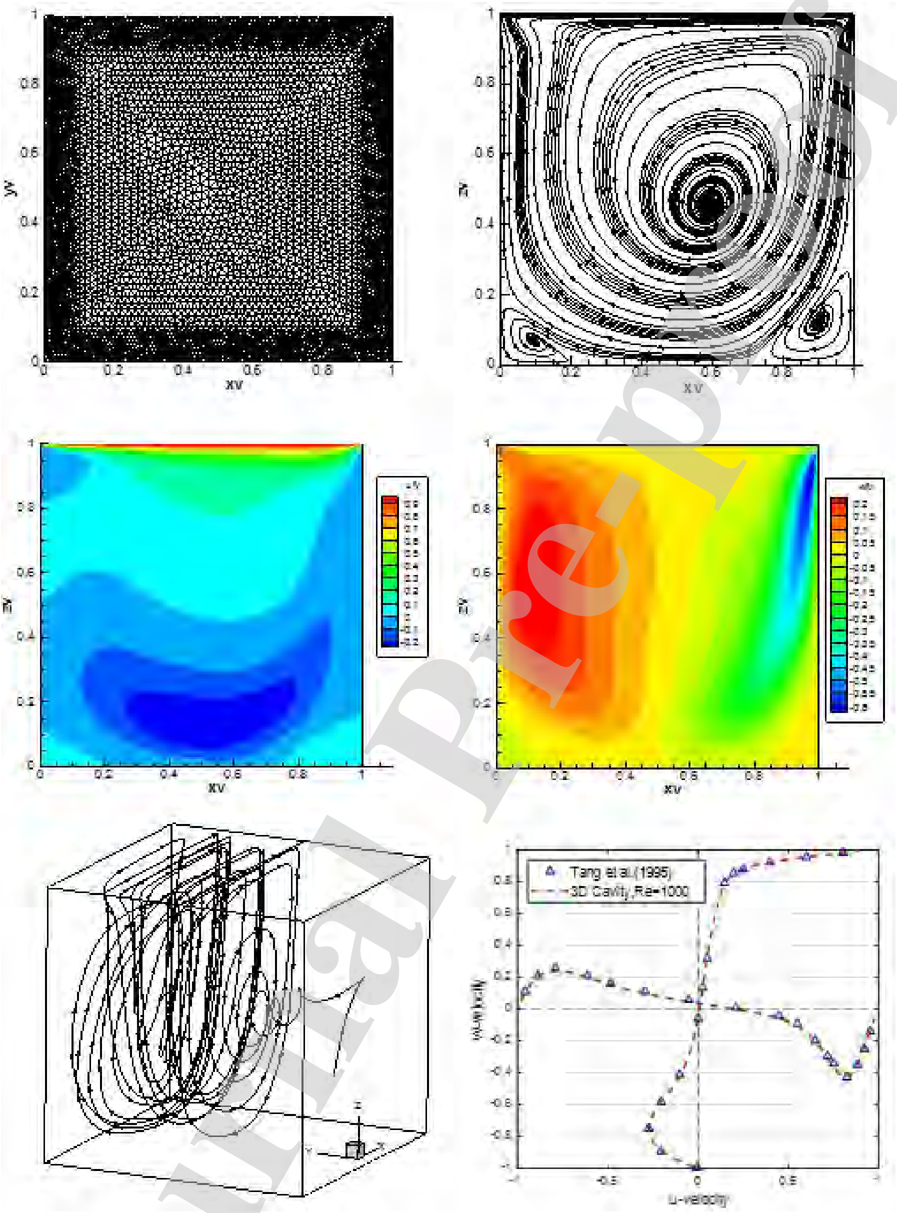

Figure 23: Contour plots of 3D cavity driven flow at $Re = 1000$. (a) Streamwise velocity; (b) Vertical velocity; (c) Profile of midsection velocity; (d) Streamlines.

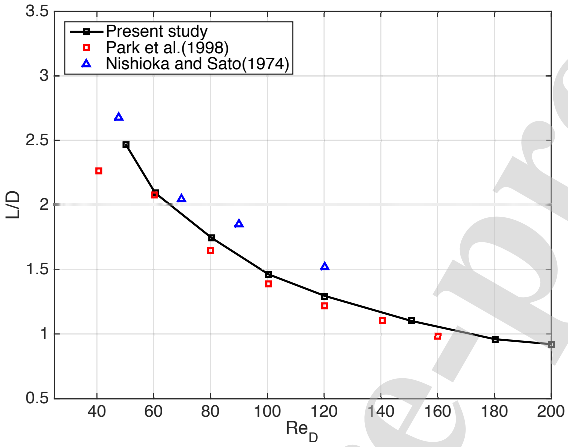

Figure 24: Evolution of the recirculation length as function of the Reynolds number.

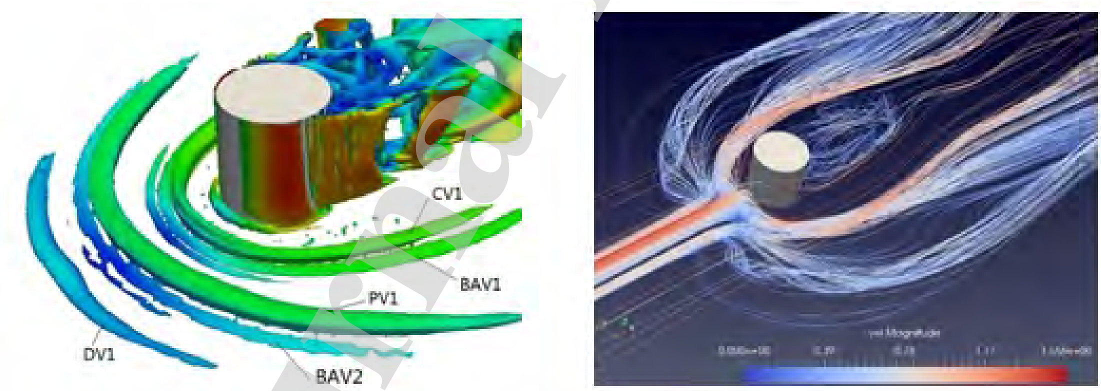

Figure 25: (a) Detailed view of the HV coherent structure; (b) and 3D streamlines.

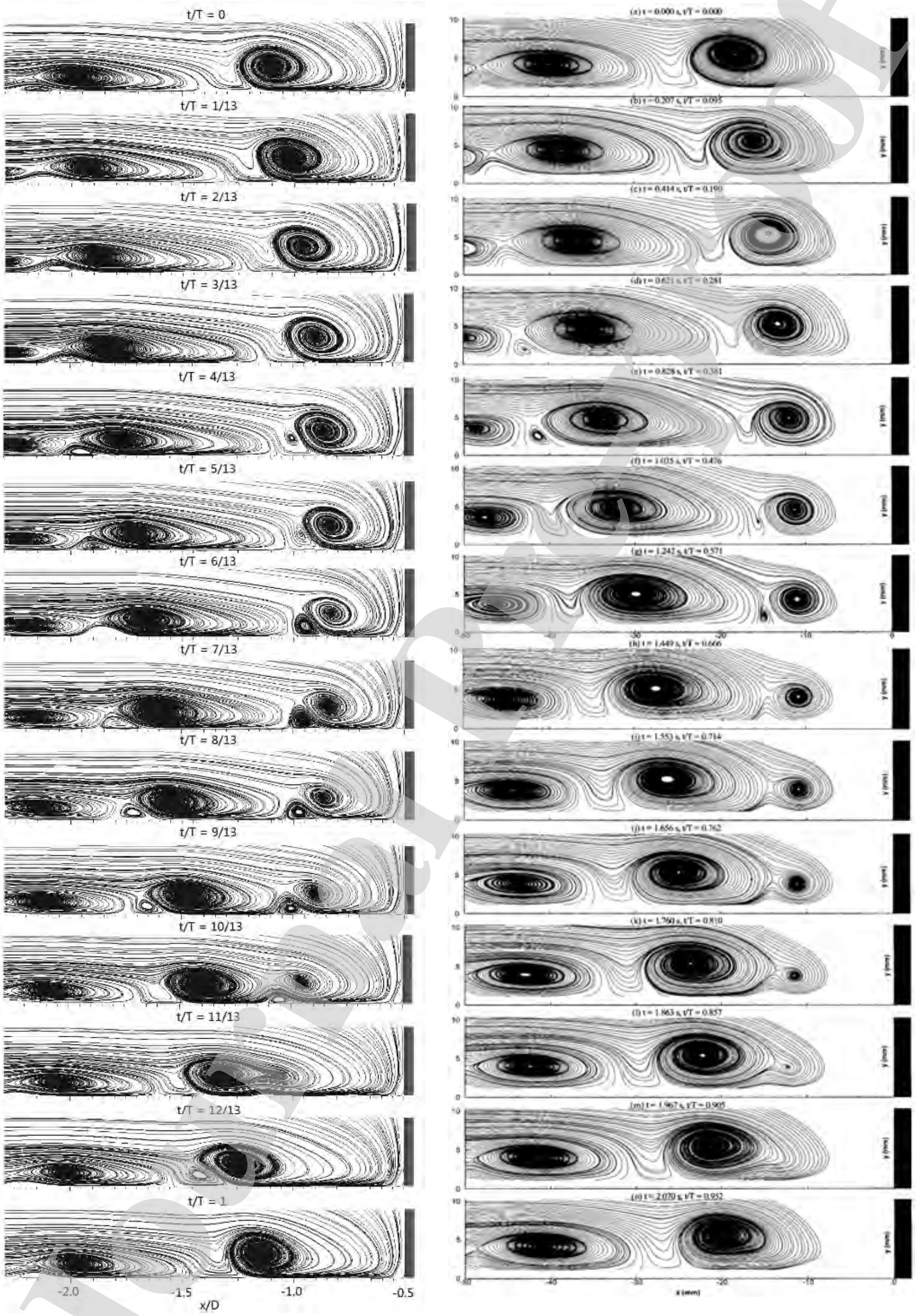

(a)

(b)

Figure 26: Streamline patterns in the upstream comparing the LES numerical results with the experiment of Lin et al. [48] at a time interval of $0.0769T$. T is the period of the breakaway cycle.

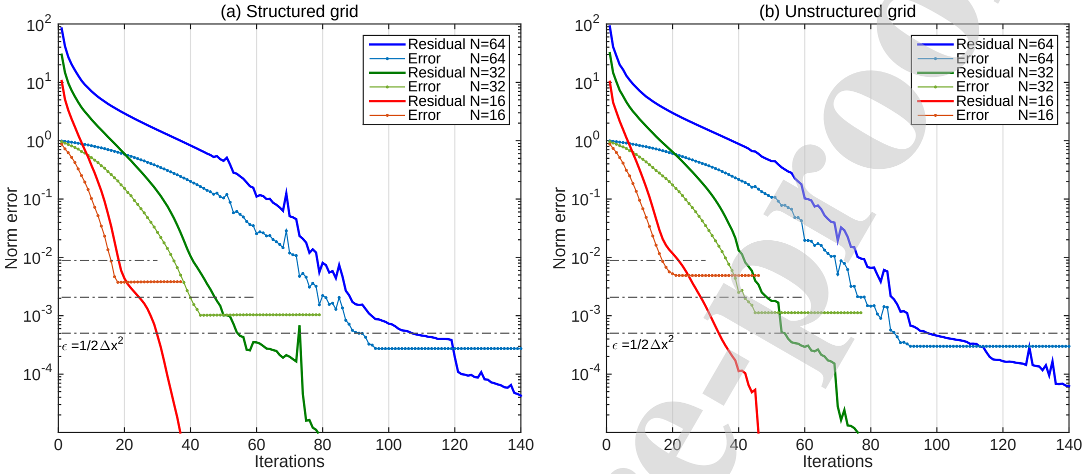

Figure 27: Convergence analysis of the BICGSTAB method for the solution of the Poisson equation using (a) structured equilateral and (b) unstructured grids. Number of iterations as function of the tolerance value and error of the finite-volume method for different grid resolutions.

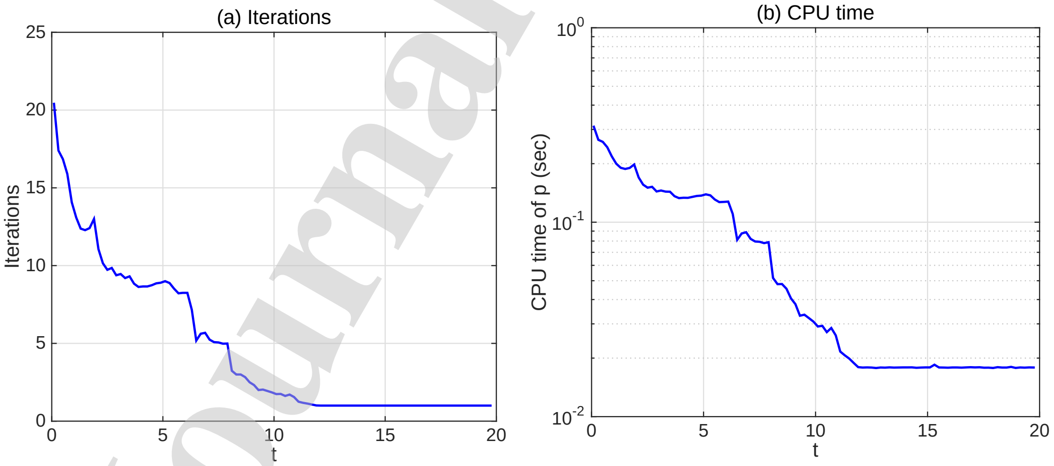

Figure 28: Convergence analysis of the BICGSTAB method for the solution of the lid-driven cavity flow test case.

An unstructured finite volume method based on the projection method combined momentum interpolation with a central scheme for three-dimensional nonhydrostatic turbulent flows

Conflict of interest

The authors declared that they have no conflicts of interest to this work. We declare that we do not have any commercial or associative interest that represents a conflict of interest in connection with the work submitted.

The authors
Dec. 21 2019